Effect of post-annealing on microstructure and electrical properties of BaTiO3 thick films grown by Aerosol Deposition (AD)

Anass Chrir, Oscar Rojas, Laurence Boyer, Olivier Durand, Pascal Marchet

Effect of post-annealing on microstructure and electrical properties of $BaTiO_3$ thick films grown by Aerosol Deposition (AD)

Anass Chrir[a,*], Oscar Rojas[b], Laurence Boyer[b], Olivier Durand[b], Pascal Marchet[a]

[a] Univ. Limoges, CNRS, IRCER, UMR 7315, F-87000 Limoges, France
[b] Center for Technology Transfers in Ceramics (CTTC), 7 rue Soyouz, 87068, Limoges, France

*Corresponding author: Anass Chrir
Email address: anass.chrir@unilim.fr
Full postal address: Centre Européen de la Céramique, 12 Rue Atlantis, 87068 Limoges, France

Abstract

In this work, we successfully deposited highly dense $BaTiO_3$ thick films at room temperature on kovar® substrates using aerosol deposition method (AD). As-deposited films exhibited non-ferroelectric behavior due to grain size effect. Post-annealing below 800 °C released residual stress without promoting grain growth for both air and argon annealing atmospheres. Hence, it enhanced relative permittivity, electrical resistivity (10^{12} Ω.cm) and reduced leakage currents (<1 µA.cm^{-2}). Annealing at 800 and 900 °C induced significant grain growth, favoring the recovery of ferroelectric properties. Grain growth was further enhanced for argon-annealed BT films. For annealing temperatures ≥ 800 °C, both air and argon annealing induced a piezoelectric behavior, clearly evidenced by the strain – field (S-E) cycles. The 900 °C argon-annealed film exhibited the highest properties, with a P_r of ~6.6 µC.cm^{-2} and a maximum strain of 0.04% under 10 kV.mm^{-1}.

Keywords:

Aerosol deposition, thick films, post-annealing, microstructure, electrical properties

1. Introduction

The research on piezoelectric materials has experienced significant growth in recent decades due to their remarkable ability to convert mechanical stress or pressure into electrical energy and vice versa. These materials offer a wide range of applications, including energy harvesters [1], pressure sensors [2], micro-actuators [3], and more.

Since the discovery of piezoelectricity in these compounds by Jaffe in 1954 [4], $PbZr_{(1-x)}Ti_xO_3$ (PZT) and PZT-based compositions have dominated the piezoelectric materials market. Indeed, PZT-based materials exhibit high piezoelectric performances, are easy to synthetize and sinter, and their properties are easily modulated by doping or chemical substitution. However, the presence of lead in compounds and its environmental toxicity raised concerns. In response, the European RoHS and WEEE directives were implemented to restrict the use of hazardous substances, including lead, in electrical and electronic devices, and to promote electronic waste recycling [5,6].

Under these directives, a concerted effort is underway to explore lead-free alternatives to PZT for piezoelectric devices. Many lead-free ceramics investigated belong to the perovskite family, of general formula ABO_3. These materials have shown promising properties that may, under specific conditions, be comparable to those of PZT-based ceramics [7–9]. Among the various perovskite compositions, the most studied include $BaTiO_3$ (BT) and its derivatives such as (Ba, Ca)(Ti, Zr)O_3 (BCTZ), (K, Na)NbO_3 (KNN), as well as alkaline-bismuth titanates like $Na_{0.5}Bi_{0.5}TiO_3$ (NBT) and $K_{0.5}Bi_{0.5}TiO_3$ (KBT), along with solid solutions based on these

compounds. In terms of performance, NBT, KNN, and BT emerge as the most promising lead-free ceramics for the replacement of PZT-based piezoceramics.

These piezoelectric materials are commonly used in bulk by ceramic forming techniques. Nevertheless, their use as thin or thick films is becoming increasingly interesting. Physical Vapor Deposition (PVD), Chemical Vapor Deposition (CVD), and screen-printing techniques have been employed to grow piezoelectric films. However, these techniques have several drawbacks: (i) they are relatively complex and need suitable chemicals (e.g. screen-printing inks), (ii) they involve high thermal energy input during deposition, and (iii) post-deposition thermal crystallization processes are required, which limits the choice of substrate materials. In addition, their film growth rate is relatively low. Among these conventional techniques, screen-printing is the most suitable for the elaboration of micrometer-thick films. However, it requires thermal treatments to crystallize and consolidate the formed layers and exhibits poor thickness control, especially below 40 µm.

An emerging deposition technique called Aerosol Deposition (AD) method offers a solution enabling at room temperature the deposition of ceramic thick film over a wide thickness range, from 1 to several hundred micrometers. This technique was developed in the late 1990s by Jun Akedo in Japan [10–12]. Over the years, AD method has gained popularity and has been adopted by a few research teams worldwide, with numerous research efforts dedicated to exploring and optimizing it.

AD device includes an Aerosol Generator (AG) connected to a Deposition Chamber (DC) which is connected to a vacuum system inducing low pressure in the DC. This method basically consists in forming a dry particle aerosol by a carrier gas injected (such as N_2, O_2, Ar, He, Air) and a vibratory effect produced in the AG. Once the aerosol is formed, the pressure difference between DC and AG results in high velocity (100-600 $m.s^{-1}$) spraying of the particles onto a substrate by a specially designed nozzle. The high kinetic energy at impact promotes crack propagation and fragmentation phenomena in the deposited powder, that give rise to new highly reactive surfaces, leading to coating consolidation/sintering. These hypothetical and more accepted mechanisms are regrouped in what Jun Akedo introduced as *Room Temperature Impact Consolidation* (RTIC) [13]. The successive particle impact, which forms the coating layers, further enhances densification due to a hammering effect. Particle size, grain size, agglomeration state and mechanical properties of the pulverized powders have a significant influence on these phenomena. To achieve the desired thickness and profile of ADM films, the starting powders must therefore be controlled by pretreatments (milling and/or thermal treatment), adjusted according to the characteristics/conditions of the ADM process (carrier gas flow, pressure in DC, and nozzle geometry).

This AD method, unique in room temperature processing, allows the formation of highly dense (>95%) nanostructured ceramic coatings in a wide thicknesses range, as well as strong adhesion to the substrate and high dielectric strength. These advantages have promoted its successfully use for depositing various materials, including oxides (PZT [14], Al_2O_3 [15], NBT-BT [16], YSZ [17]), nitrides (AlN [18]), carbides (SiC [19]), borides (MgB_2 [20]), MAX phases (Ti_3SiC_2 [21,22]), and composites (LSM-YSZ [23], Al_2O_3-PTFE [24], TiO_2-Cu [25], SiC-$MoSi_2$ [26]). Thick $BaTiO_3$ (BT) films have also been successfully deposited by AD method on copper [27], glass slide [28], alumina (Al_2O_3) [29], stainless steel (SUS) [30], yttria-stabilized zirconia (YSZ) [31], and $SrTiO_3$ [32] substrates. Although the AD method is advantageous, the impact fragmentation of the particles causes a significant grain size reduction in the films, which alters the piezoelectric functional properties [13,16,33]. Consequently, ceramic substrates have been widely privileged due to their compatibility with $BaTiO_3$, in terms of coefficient of thermal expansion (CTE) , which facilitates the thermal treatment of the deposited films. Some metallic substrates such as SUS substrates, although

having a higher CTE than BT, have also been studied as they offer good high-temperature oxidation resistance.

Most of these studies have mainly focused on the dielectric properties of $BaTiO_3$ films, aiming to integrate them as passive components in printed wiring boards or for multilayer ceramic capacitors (MLCC) [34,35]. However, ferroelectric and piezoelectric properties have been scarcely discussed and few papers report the ferroelectric properties of BT films deposited by AD [36–39]. Generally, lower properties are reported when metallic substrates are used, which can be attributed not only to the microstructure of BT films but also to compressive stress induced by CTE mismatch between the BT films and metallic substrates. In contrast, the weak tensile residual stress generated by using YSZ ceramic substrates shows a positive effect on electrical properties of BT films [31,37].

Nevertheless, the effect of annealing conditions has not been extensively studied. Indeed, most reported post-deposition annealing treatments were performed in air atmosphere using relatively low (≤ 500 °C) or high temperatures (≥ 1000 °C), but without comprehensive comparative studies under different annealing conditions. Likewise, compared to the use of YSZ substrates, the induction of higher tensile residual stress in the BT films by using rather low CTE metallic substrates like kovar® remains unexplored. Additionally, brittle ceramic substrates should be ruled out when considering energy harvesting applications using AD-deposited BT films. Indeed, for such applications, it becomes imperative to use flexible and thin substrates to adjust the desired piezoelectric functionality. While polymer substrates offer high flexibility, they are not compatible with thermal post-annealing, restricting their use to lift-off transferred ferroelectric films only [40]. Existing research on AD-ferroelectric films focuses on thick metallic substrates (e.g., 1 mm-thick 304SUS stainless steel substrates [33,39,41]). Hence, thin and flexible metal substrates emerge as a promising option, combining the needed flexibility with the ability to withstand thermal post-annealing of AD films.

Therefore, the aims of the present study are: (i) to deposit $BaTiO_3$ thick films on flexible and relatively thin kovar® (Fe54/Ni29/Co17) substrates, (ii) to evaluate the microstructural evolution and electrical properties of the annealed BT films under two atmospheres (air and argon), and (iii) to gain further insights into the influence of tensile residual stress on the electrical properties of $BaTiO_3$ thick films using kovar® substrates.

2. Experimental procedure

2.1. Aerosol Deposition process

Commercial $BaTiO_3$ powder (Alfa Aesar, 99%) was used to deposit $BaTiO_3$ thick films by Aerosol Deposition (AD) method. $BaTiO_3$ films were deposited on 1 mm-thick glass slides and 125 µm-thick kovar® sheets (Goodfellow, glass sealing alloy, Fe54/Ni29/Co17) using either helium (He) or nitrogen (N_2) as carrier gases. Glass slides substrates were initially used in preliminary tests to adjust (by vibration intensity and carrier gas flow) the particle aerosol generation before deposition on kovar® sheets. The required thickness of the ADM films in this study ranged from 10 to 100 µm, as is typical for piezoelectric devices.

The AD apparatus scheme used in this work is depicted in Figure 1. The aerosol generator (AG) is fitted with a vibration plate to induce the dry BT particle aerosol with support of the carrier gas flow. Gas flow rates of 5-20 $L.min^{-1}$ for He and 5-15 $L.min^{-1}$ for N_2 were injected into the aerosol generator (AG). The resulting dry aerosol flow was sprayed into the deposition chamber (DC) through a nozzle positioned at 5 mm from the substrate. Vacuum

pressure in the AG was maintained between 10-80 kPa, while the pressure in the DC ranged from 0.05-1 kPa. $BaTiO_3$ thick films of 5 mm x 10 mm were deposited by scanning speed of 1.5 $mm.s^{-1}$ using motorized plates. The films formed were then subjected to thermal post-annealing in an electric furnace at various temperatures for 3 h either in air or argon flow.

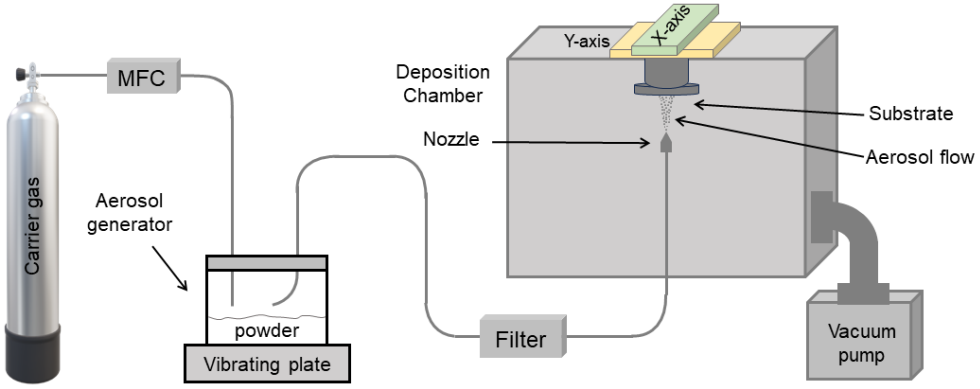

Figure 1. Scheme of the AD apparatus (one-column, color online)

2.2. Characterization techniques

The thickness profile of $BaTiO_3$ thick films was determined using a stylus profilometer (Veeco Dektak-8). The crystal structure analysis of the films was performed by X-Ray Diffraction (XRD) (Bruker D8 Advance X-Ray diffractometer) in Bragg-Brentano geometry. The XRD patterns were obtained for 2Θ angles ranging from 20° to 80° (step size of 0.02° and 0.2 s per step) using Cu Kα wavelength ($\lambda_{k\alpha1}$ = 1.5406 Å). Based on the Full Width at Half Maximum of the XRD peaks (FWHM), we calculated the crystallite size and microstrain within BT films by using the Williamson-Hall method. Raman spectroscopy was used to examine the local structure of the BT films and verify changes in crystalline symmetry and internal stress. Raman spectra were recorded in the spectral range of 200–900 cm^{-1} using T64000 HORIBA Jobin–Yvon spectrometer operating in the triple subtractive configuration with a wavelength of 514.5 nm. For the comparative study on annealed BT films, the obtained Raman spectra were subjected to normalization (total area normalization) and baseline correction (linear correction) procedures. Elemental analysis and cross-section observations were performed using a scanning electron microscope (SEM, Zeiss Crossbeam 550) coupled with Focused Ion Beam (FIB) and Energy-Dispersive X-ray Spectroscopy (EDS). ImageJ software was used to process the SEM-FIB images of the BT films in order to determine their densification rate [42]. High-resolution Transmission Electron Microscope (TEM) observations were carried out (JEOL JEM 2100F) to validate the microstructural findings obtained from XRD data and to visualize the microstructural changes due to the annealing treatment.

Electrical measurements on the $BaTiO_3$ films were performed using a ferroelectric analyzer (TF 2000, aixACCT Systems GmbH). Silver electrodes were deposited on the top surface of the films using colloidal silver. Prior to electrical measurements, the BT films were poled at 5 $kV.mm^{-1}$ for 30 min at room temperature. The Polarization-Electric field (P-E) and Strain-Electric field (S-E) loops were measured using a triangular wave with an electric field amplitude of 10 $kV.mm^{-1}$ and a frequency of 10 Hz. To evaluate the reliability of the annealed BT films, fatigue measurements were performed by measuring the P-E loops for 10^6 cumulative cycles using the same conditions as P-E loops. Before each measurement of a P-E cycle, a bipolar switching pulse with a frequency of 100 Hz and an electric field corresponding to 2.5 times the coercive field (E_c) of the examined film is applied. Additionally, leakage current density measurements were performed using a maximum DC voltage of 1 kV applied to the 100 µm-

thick films, which is equivalent to a field of 10 kV/mm. The voltage increment was set at 50 V with a dwell time of 2 seconds at each step.

3. Results and discussion

3.1. As-deposited films

3.1.1. Thickness measurement

Figure 2 presents an example of a homogeneous $BaTiO_3$ thick film profile obtained after optimizing particle aerosol generation. BT films exhibit a pyramidal shape, particularly when helium is used as the carrier gas. This pyramidal form is a consequence of the divergence of the aerosol jet, which can be minimized by reducing the distance between nozzle and substrate, or using a deposition mask. If the homogeneity of the profiles varies as a function of nozzle, carrier gas, and powder characteristics, uniform thicknesses are generally associated with stable and homogeneous aerosol flow. Therefore, the quality of the dry particle aerosol can be qualitatively assessed based on the thickness profile.

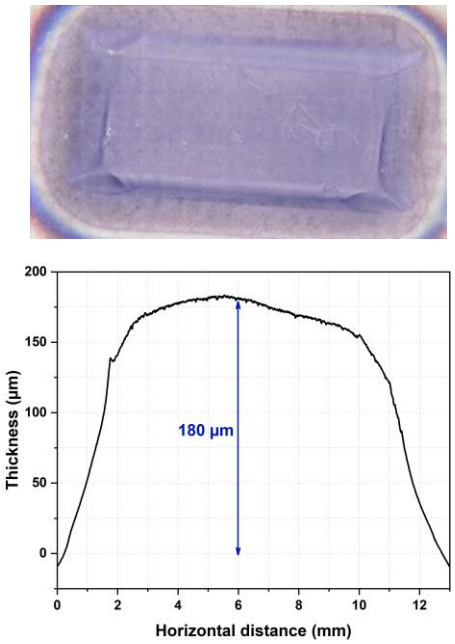

Figure 2. Surface of $BaTiO_3$ thick film (captured by numerical optical microscopy) and corresponding thickness profile measured by stylus profilometer (one-column, color online)

The evolution of film thickness with respect to the flow rate of the two carrier gases was evaluated (Fig. 3). The thickness of $BaTiO_3$ thick films increases with increasing flow rate of helium carrier gas injected into the aerosol generator. A similar trend is observed for the lowest nitrogen flow rates, while the film thickness tends to decrease for higher flow rates. This behavior is attributed to particle aerosol stability during AD coating formation. While a particle-rich aerosol is favored by increasing the vibration effect and the carrier gas flow, an excessive concentration of BT particle aerosol and gas molecules (particularly large, e.g., N_2) in the spray nozzle induces an overpressure in the AG. This causes settling and agglomeration of the $BaTiO_3$ powder, resulting in a significant particle aerosol depletion. However, particle and gas molecule saturation at the spray nozzle occurs more gradually when using helium carrier gas. The smaller size of the helium molecule facilitates its flow between particles favoring both powder deagglomeration and efficient particle flow, even in more particle-rich aerosols as the helium volumetric flow rate increases.

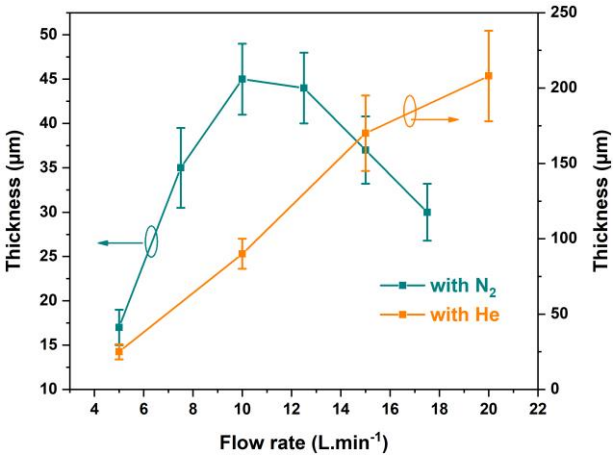

Figure 3. $BaTiO_3$ film thickness evolution for different helium and nitrogen flow rates (one-column, color online)

These BT thick films were formed in all cases in less than 5 min, reaching a maximum deposition rate of ~ 50 µm.min^{-1} (equivalent to 1 µm.mm².min^{-1}). This is a considerably high value compared to conventional methods (CVD, PVD), where the coating rate typically ranges from 0.01 to 0.05 µm.min^{-1} [43].

3.1.2. Cross-sectional FIB-SEM observations

The high density of aerosol-deposited films is one of their distinguishing characteristics. The densification of the BT films was assessed in this study through cross-section images obtained by FIB-SEM (Fig. 4). The results clearly confirm the occurrence of room temperature densification, resulting in the formation of highly dense BT thick films. The relative density of all the BT films examined using ImageJ software is over 98,5 Area %. However, some stacking defects are observed in the cross-section images. Differential densification along the thickness direction is also apparent, confirming the phenomenon known as "hammering effect" reported in the literature for AD films [13]. Indeed, the initial deposited layers (those closest to the substrate) experience further densification due to the impact of subsequent particles. As a result, the film density is higher at the film-substrate interface and gradually decreases towards the film surface, which generally has more structural defects.

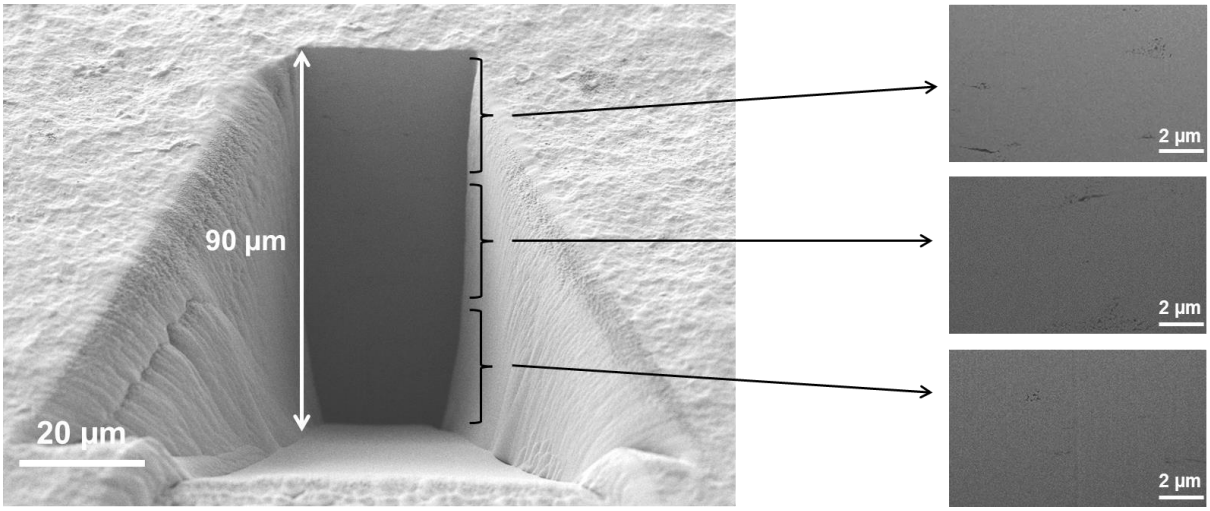

Figure 4. Cross-section FIB-SEM images of the as-deposited $BaTiO_3$ thick film (two-column, color online)

Additionally, the surface morphology of the BT films displays surface cratering. These surface craters observed on AD films are the result of particle impact during the deposition process, in agreement with the surface morphology reported in the deposition of various materials using AD [44].

3.1.3. X-ray diffraction

Two typical XRD patterns of BT films formed with nitrogen (N_2) and helium (He) as carrier gases are shown in Figure 5. Both XRD patterns demonstrate that the as-deposited BT films have a crystallized perovskite structure and no significant influence of the carrier gas on the XRD patterns is observed. Furthermore, the occurrence of an amorphous phase in the film cannot be excluded. The observed peak positions closely match those reported for tetragonal $BaTiO_3$ (JCPDS #05-0626), with a slight shift towards lower angles. In addition, as commonly observed for AD films, a broadening of the XRD peaks is evidenced. This broadening can be attributed to both reduced crystallite size due to particle fragmentation, and significant microstrain introduced during high-speed particles impact, as it has already been reported [13]. Because of this peak broadening, the symmetry of the perovskite phase (cubic or tetragonal) could not be determined from the XRD patterns. Indeed, the (200) cubic peak splitting into (002) and (200) peaks, characteristic of tetragonal symmetry, could not be resolved, giving the XRD patterns a pseudo-cubic appearance (Fig. 5.b).

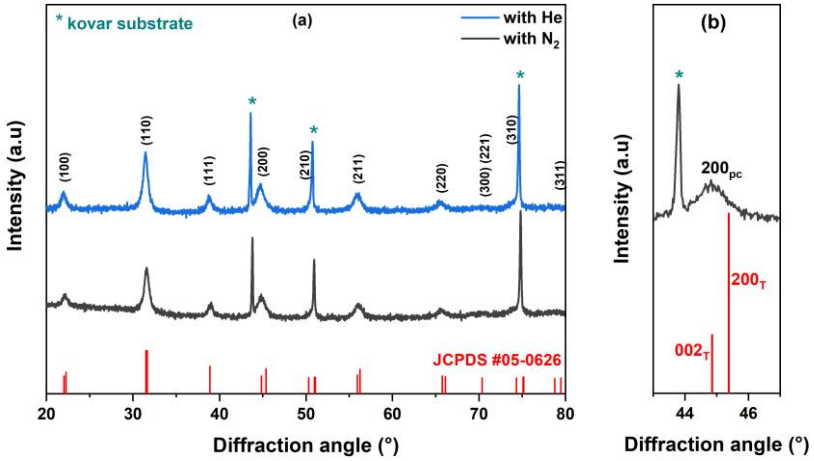

Figure 5. (a) XRD patterns of as-deposited BT films using helium and nitrogen carrier gases and (b) zoom on the (200) peak (the peak indexing in the upper part of the figure corresponds to pseudo-cubic symmetry, JCPDS card is for $BaTiO_3$ tetragonal symmetry) (one-column, color online)

3.1.4. Raman spectroscopy

As reported hereabove, the XRD analysis did not provide a definitive assessment of the symmetry of the deposited $BaTiO_3$ (BT) phase. In contrast, Raman spectroscopy allows differentiation between cubic and tetragonal $BaTiO_3$ symmetries, even for nano-sized grains. Therefore, Raman spectroscopy acquisitions were performed on the raw powder and for deposited $BaTiO_3$ films (Figure 6).

The Raman spectra of the as-deposited films show four main bands around 270 cm^{-1}, 305 cm^{-1}, 515 cm^{-1}, and 720 cm^{-1}. While the cubic $BaTiO_3$ phase is theoretically Raman inactive (centrosymmetry), the observed broad Raman bands centered at 270 cm^{-1} and 520 cm^{-1} have been previously observed above the tetragonal-to-cubic phase transition temperature in $BaTiO_3$ [45]. The persistence of these bands has been attributed to the disorder of Ti atoms in the cubic phase [46]. Therefore, these Raman bands could be present in both tetragonal and cubic phases. On the contrary, the broad Raman bands centered at 305 cm^{-1} and 720 cm^{-1} can be unambiguously assigned to the tetragonal phase. Consequently, the 270 cm^{-1} (A_1(TO)) and 515 cm^{-1} (E(TO), A_1(TO)) bands cannot be considered for symmetry identification, while

the tetragonal symmetry of $BaTiO_3$ is typically identified based on the occurrence of the characteristic 305 cm^{-1} (E(LO + TO), B_1) and 720 cm^{-1} (E(LO), A_1(LO)) bands [47,48]. Therefore, these results clearly confirm the conservation of the tetragonal (ferroelectric) $BaTiO_3$ symmetry in the aerosol-deposited $BaTiO_3$ films.

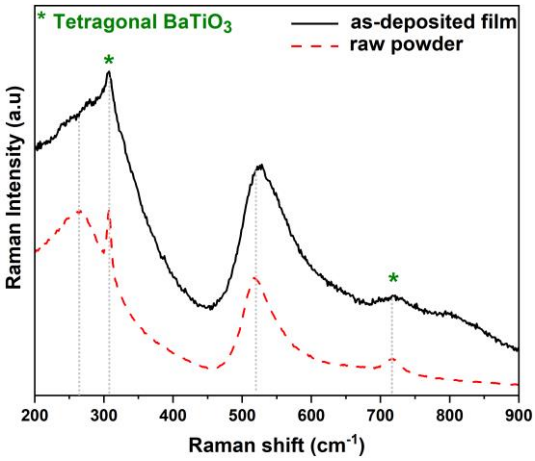

Figure 6. Raman spectra for deposited $BaTiO_3$ films and raw powder (one-column, color online)

A comparison between the two spectra reveals some differences attributed to the influence of crystallite size and residual stress within the BT films. Notably, the Raman band originally located at 515 cm^{-1} undergoes a shift towards higher wavenumbers. This shift has previously been explained by Sakashita et al. [49] as a consequence of internal stress in $BaTiO_3$, with a shift reported at 519 cm^{-1} for an applied stress of 60 MPa [49]. Here, the Raman band shifts to 526 cm^{-1}, indicating high internal stresses in the as-deposited BT films. This result aligns well with the general tendency reported in structural studies of aerosol-deposited films, in which highly distorted crystal lattices have been found [50]. In addition, the Raman band at 305 cm^{-1} in the as-deposited film exhibits broadening while the intensity of the 270 cm^{-1} band decreases significantly. These differences can be attributed to the influence of the grain structure, as they match with similar observations reported by Hoshina et al. [51] for $BaTiO_3$ nanoparticles with sizes below 30 nm [51]. This finding confirms that the aerosol deposition (AD) process leads to a reduction in grain size, resulting in grain sizes smaller than 30 nm.

3.1.5. Electrical properties :

The P-E loops of an as-deposited BT film before and after poling were measured to estimate the impact of the AD process on the electrical properties of the films (Fig. 7a). The polarization curve does not reach saturation at high electric fields and no evidence of polarization switching is observed. The P-E loops obtained display a linear (lossy) dielectric-like behavior, indicating the absence of ferroelectricity in the as-deposited AD films. The absence of ferroelectric hysteresis can be attributed to the size effect. Indeed, a critical grain size has been described in $BaTiO_3$ below which the long-range correlation between ferroelectric domains is lost, resulting in the loss of ferroelectric ordering at the macroscopic scale [52]. The disappearance of the tetragonal crystal structure has also been reported for low grain sizes, with the crystal structure of $BaTiO_3$ particles becoming cubic (paraelectric) [51]. In our case, Raman spectra confirmed the presence of tetragonal $BaTiO_3$, indicating that the lack of ferroelectricity is likely not due to the local symmetry of the as-deposited $BaTiO_3$ films, but more coming from the absence of ferroelectric ordering between nano-sized domains. These results are consistent with previous findings on as-deposited films, where macroscopic ferroelectricity properties was rarely demonstrated, mainly limited to Pb-based piezoelectric materials [53].

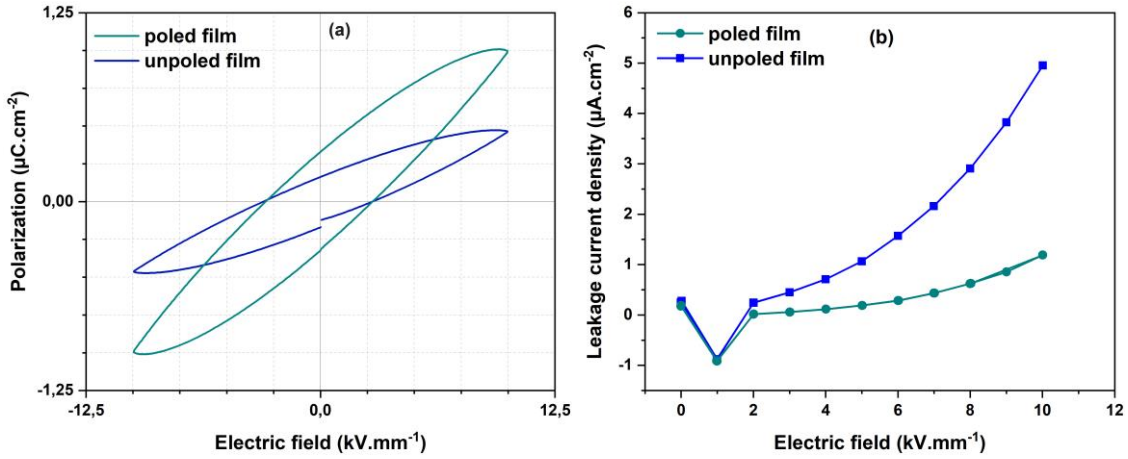

Figure 7. (a) Polarization-Electric field loops and (b) leakage current measurements for as-deposited $BaTiO_3$ film (two-column, color online)

In addition, the poling operation of the $BaTiO_3$ films changed the P-E curve slope (i.e. relative permittivity), which becomes higher after poling. Consequently, the calculated relative permittivity derived from the P-E loops is approximately 51 for the unpoled sample and 113 for the poled sample. This behavior evidences the existence of ferroelectric nanodomains in the as-deposited BT films, which can realign by a poling process. This domain realignment contributes to increase the overall polarization of the film, thus enhancing its relative permittivity.

Figure 7b depicts the leakage current density measured for the same sample before and after the poling treatment. No dielectric breakdown occurred under an electric field of 10 $kV.mm^{-1}$. The leakage current density value is 5 $\mu A.cm^{-2}$ for the unpoled sample and is reduced to 1 $\mu A.cm^{-2}$ after poling. Furthermore, the electrical resistivity of the as-deposited BT films, measured under a DC field, ranges from 10^9 to 10^{10} Ω.cm, increasing from $2.4x10^9$ to $6.5x10^9$ Ω.cm respectively for the unpoled and the poled sample. The leakage observed in the BT films can be predominantly attributed to oxygen vacancies formed during the particle fragmentation phenomenon involved in the AD process. The leakage reduction in poled films can be linked to the enhanced domain alignment. Domain alignment results in reduced internal electric fields and fewer opportunities for leakage paths, which may offset the oxygen vacancy impact.

3.1.6 Summary concerning as-deposited films

To sum up, the characterizations performed on as-deposited BT films confirm the deposition of high density BT thick films, while conserving their tetragonal perovskite symmetry. Grain size reduction and high internal stresses within BT films are evidenced. Due to low grain size of the as-deposited films, they demonstrate dielectric linear-like behavior justifying the necessity of post-annealing treatment developed in the next sections. Interestingly, the relative permittivity of the films and the leakage currents can respectively be increased and reduced by poling, which aligns well with the observed ferroelectric tetragonal symmetry and suggests the possible presence of polar nanodomains in the as-deposited BT films. The electrical resistivity of the BT films is promising, falling within the range of 10^9-10^{10} Ω.cm. As for dielectric strength, BT films can withstand a DC field of 10 $kV.mm^{-1}$ while maintaining a relatively low leakage current density.

3.2. Annealing in air atmosphere

To investigate the possibility of recovery of ferroelectric properties through thermal treatment, annealing tests were performed in an electric furnace to examine the influence of annealing

temperature and atmosphere on the microstructural features and electrical properties. The post-deposition treatment of AD films aims to: (i) crystallize any amorphous phases formed during particle impact, (ii) release the compressive residual stress caused by the deposition mechanism and (iii) promote grain growth in order to restore the long-range correlation between ferroelectric domains.

3.2.1. Annealing parameters

While the precise temperature for volume diffusion activation in $BaTiO_3$ requires further investigation, previous studies have reported volume diffusion at 650 °C and significant cross grain boundary diffusion around 750 °C [54]. With these considerations in mind, we chose two ranges of annealing temperatures as following:

- Relatively low temperatures (500 and 700 °C): Initially, low temperatures were tested, as higher grain surface area was suspected to reduce the energy required for sintering of AD films and promote grain growth within this temperature range. Moreover, annealing at low temperatures was expected to relieve residual stress and potentially enhance film properties, while preserving the mechanical integrity of the films (minimization of thermal stress).
- Higher temperatures (800 and 900 °C): In this temperature range, grain growth is more likely to occur, which can potentially result in recovery of the ferroelectric and piezoelectric properties.

Significantly, even a slight coefficient of thermal expansion (CTE) mismatch between the metallic kovar® substrate and the $BaTiO_3$ ceramic film can induce high interfacial stress during thermal treatment. In order to reduce the risk of film delamination and cracking, relatively low heating and cooling rates were used.

Using these carefully chosen parameters, our qualitative observations revealed the preservation of substrate-film cohesion throughout the annealing process. Notably, films did not delaminate, even in the presence of oxidized substrates. Furthermore, the annealed films presented no observable cracks. Moreover, the as-deposited BT films exhibited a bending direction indicative of compressive stress, which was significantly reduced after annealing. This resulted in relatively flat films, particularly for 900 °C annealing.

3.2.2. Elemental interdiffusion analysis

Energy-dispersive X-ray spectroscopy (EDS) was employed to analyze, on the cross-section prepared by FIB, the elemental interdiffusion between the substrate and the $BaTiO_3$ layer annealed specifically at 800 °C. Two EDS analysis were performed, one within the BT film (Fig. 8.a) and another within the Kovar® substrate section (Fig. 8.b). Low atomic percentages of Ba and Ti in the substrate section are notably detected, while Fe, Ni, and Co elements are identified in the film section. The proportion of metallic elements detected in the substrate section analyzed is quite different from the nominal composition of kovar® (Fe54/Ni29/Co17). Hence, it is important to note that interpretation of these EDS data are for comparative purpose only, since obtaining precise quantitative measurements would require more advanced analytical techniques.

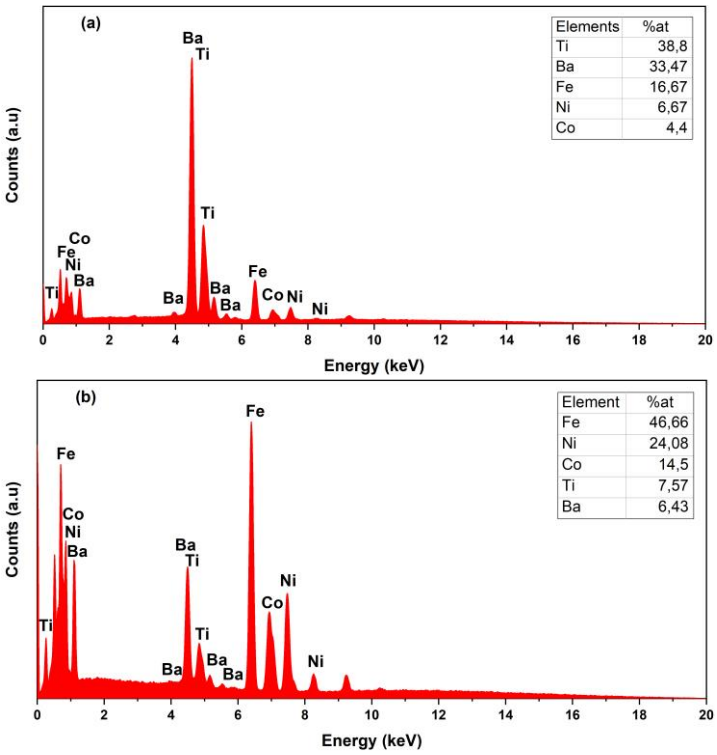

Figure 8. EDS elemental analysis results inside (a) film section and (b) substrate section for annealing at 800 °C in air (one-column, color online)

A 13 µm deep EDS profile line within the BT film section towards the substrate was selected to analyze Fe, Ba and Ti elemental evolution (Fig. 9). The results reveal a higher iron percentage close to the substrate-film interface (point B), which gradually decreases with increasing distance from the substrate-film interface (point A).

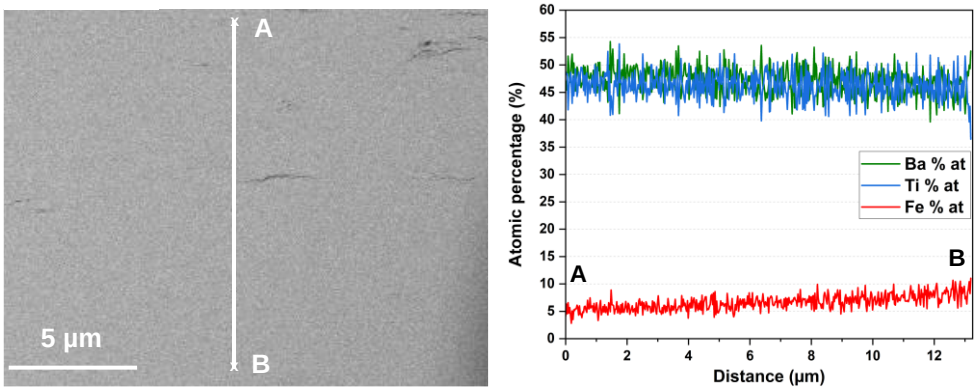

Figure 9. Chemical element profile line measured by EDS for air-annealed BT films at 800 °C (point B is close to the substate film interface and point A close to the top surface of the film) (one-column, color online)

EDS analyses of kovar substrate and BT film (Fig. 8 and Fig. 9) confirm chemical species interdiffusion, especially for Fe, across the film-substrate interface during the thermal treatment under air atmosphere. This explains the presence of these chemical elements even at the top surface of the BT film, which can have a significant impact on the electrical properties.

3.2.3. Structural and microstructural analysis

TEM analysis was performed to visualize the microstructural changes induced by the thermal treatments. Figure 10 shows TEM images comparing the as-deposited film and the film

annealed at 900 °C. The as-deposited film exhibits spherical crystallites with nanometric sizes ranging from 5 to 25 nm. No discernible correlation in crystallographic orientation is observed between neighboring crystallites, and the grain boundaries are not distinguishable.

In contrast, the annealed film reveals faceted grains with sizes ranging from 30 to 100 nm, indicating heat treatment effect on grain growth. Notably, well-defined grain boundaries are visible, which are absent in the as-deposited film.

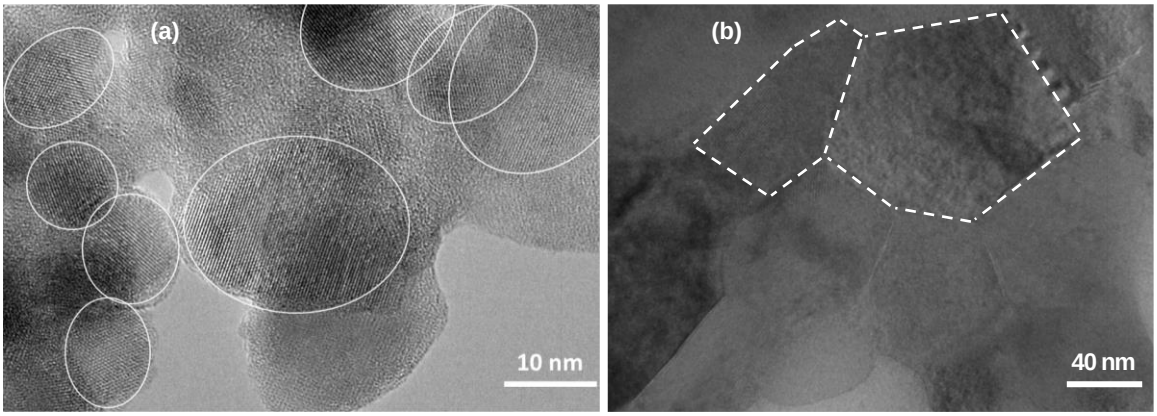

Figure 10. TEM images comparing the microstructure of the BT film (a) as-deposited and (b) annealed at 900 °C in air (two-column, color online)

The structural changes in the annealed $BaTiO_3$ (BT) films were further investigated by XRD (Fig. 11.a). Some XRD peaks of Fe, Ni and Co oxides are formed during the thermal annealing in air, confirming the oxidation of the kovar® substrate. The increase in annealing temperature induces an increase in the intensity of these metallic oxides. As for BT films, an evident effect on the crystallinity of $BaTiO_3$ phase (Fig. 11.b: intensity increase and reduction of FWHM), without decomposition into secondary phases.

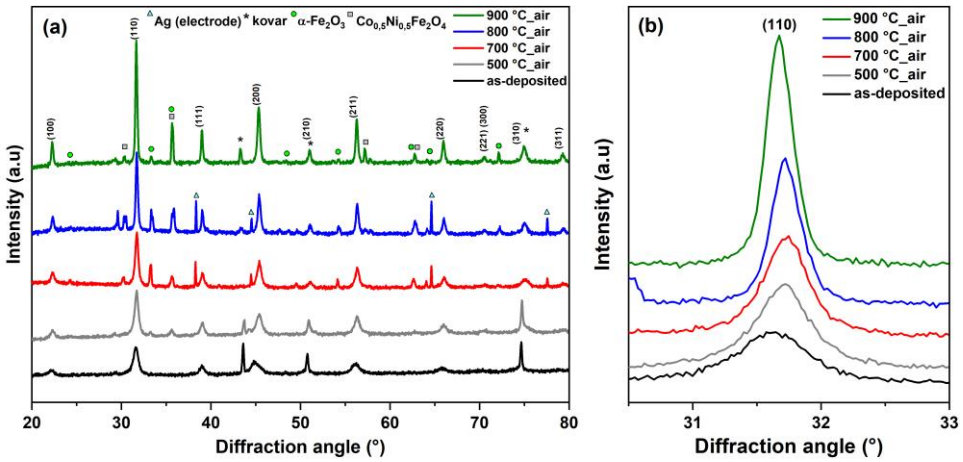

Figure 11. (a) XRD patterns of air-annealed BT films (b) zoom on (110) peak (two-column, color online)

Therefore, the Williamson-Hall method was employed to estimate the crystallite size and microstrain of the different BT films (Table 1). The calculated values indicate that annealing at 500 and 700 °C mainly affects the microstrain values, while the crystallite size remains unchanged. Compared to the as-deposited film, a 51 and 71% reduction in microstrain occurs in films annealed at 500 and 700 °C respectively. By increasing the annealing temperature to 800 and 900 °C, microstrain is further reduced to 96% (almost to no microstrain) and grain growth is promoted. For the highest annealing temperature (900 °C), the achieved maximal

crystallite size is approximately 36 nm. This value matches well with the grain sizes observed by TEM (Fig. 10). The limited grain growth can be attributed to the relatively low annealing temperatures of this study (chosen to limit substrate oxidation and risk of delamination) compared to those typically used (>1000 °C) for $BaTiO_3$ ceramics [55].

Table 1. Crystallite size and microstrain analysis of BT films annealed in air atmosphere

Annealing temperature	Crystallite size (nm)	Microstrain (%)	Microstrain evolution (%)
As-deposited	26.2 ± 2.5	0.55 ± 0.11	0
500 °C	25.7 ± 1.9	0.26 ± 0.06	- 51
700 °C	26.2 ± 1.5	0.15 ± 0.03	- 71
800 °C	34.0 ± 1.0	0.04 ± 0.01	- 93
900 °C	36.0 ± 1.0	0.02 ± 0.01	- 96

In addition to the XRD results, Raman spectroscopy was also performed. Figure 12 displays the results obtained for the raw powder, as-deposited film, and air-annealed BT films. The Raman spectra of the air-annealed BT films shows the same Raman bands of the as-deposited film, confirming the conservation of tetragonal $BaTiO_3$ structure. However, the Raman band at 515 cm^{-1} exhibits a noticeable shift towards lower wavenumbers as the annealing temperature increases. Furthermore, the annealing temperature promotes sharper bands at ~ 305 cm^{-1}.

Previous studies have reported a correlation between internal stresses in $BaTiO_3$ and the 515 cm^{-1} Raman band shift [49]. The shift towards higher wavenumbers is associated with an increase in internal stress. Therefore, the 515 cm^{-1} Raman band shift toward lower Raman wavenumbers indicates stress release in the air-annealed BT films, converging to the position of raw $BaTiO_3$ powder after annealing at 900 °C (Fig. 12b). This finding is consistent with the Williamson-Hall analysis, which demonstrate a microstrain decrease with increasing annealing temperature (Table 1). Meanwhile, the sharpening of the 305 cm^{-1} Raman band in the air-annealing BT films is associated with grain growth, as deduced from Raman studies of $BaTiO_3$ with decreasing grain sizes [51].

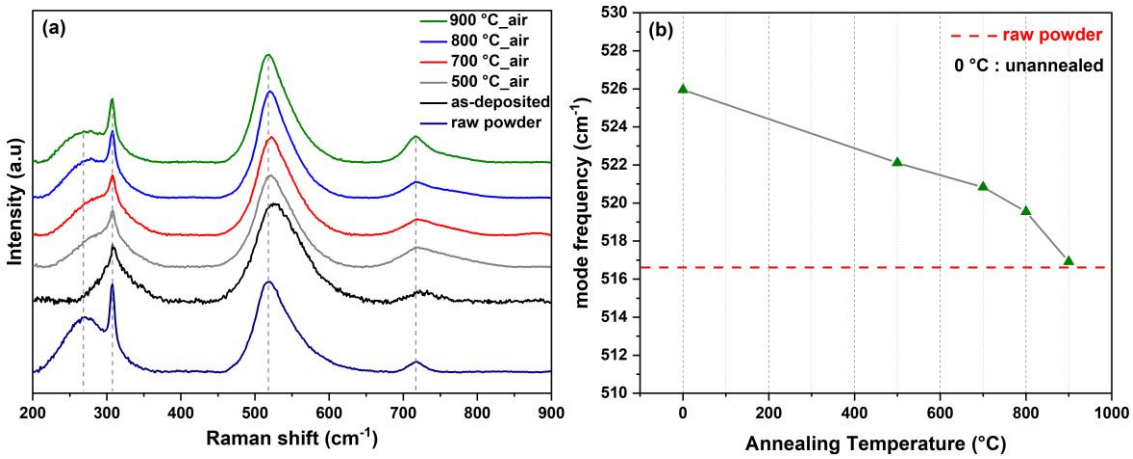

Figure 12. (a) Raman spectra of air-annealed BT films and (b) 515 cm^{-1} Raman mode shift (two-column, color online)

3.2.4. Electrical properties

The air annealing treatment of BT film, aiming the recovery of the ferroelectric properties, showed an effective influence on the P-E loop response (Fig. 13). Similarly to the as-deposited one, the BT film air-annealed at 700 °C exhibits a linear behavior without polarization switching. In contrast, films annealed in air at 800 and 900 °C present P-E loops clearly associated to ferroelectric behavior, since the electric field reversal induces a polarization switching. Furthermore, the maximum polarization (P_{max}) increases significantly, reaching maximum values close to 12.5 µC.cm^{-2} for both temperatures. However, the film annealed at 800 °C demonstrates higher remnant polarization (P_r) with a value of ~5.7 µC.cm^{-2}, compared to ~2.6 µC.cm^{-2} of those annealed at 900 °C.

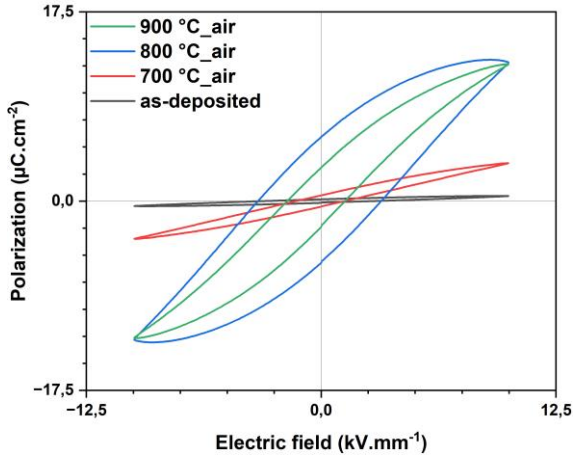

Figure 13. Polarization-Electric field loops for air-annealed BT films (one-column, color online)

These results demonstrate that stress release by annealing at 700 °C, as observed by XRD and Raman analysis, enhance the electrical properties of the BT films. However, the absence of grain growth hinders ferroelectricity even if 8 times higher P_{max} is achieved. In contrast, grain growth induced at 800 and 900 °C annealing results in ferroelectricity recovery. The combined effect of grain growth and microstrain reduction is logically associated to increased P_r. However, the high field behavior in BT film annealed at 800 °C (P tending to decrease with increasing E) demonstrate the presence of structural defects (mainly oxygen vacancies) due to deposition mechanism. Increasing the annealing temperature promotes oxygen re-incorporation within BT films, which explains the reduction of losses at 900 °C compared to 800 °C.

The strain-electric field S-E cycle measurements (Fig. 14) show a low amplitude and irregularity for BT films air-annealed at 700 °C. In contrast, the S-E loops for 800 and 900 °C annealing show a piezoelectric displacement response to the applied electric field, with increased strain values. These results correspond well with the findings by ferroelectric measurements, as the ferroelectric and piezoelectric behavior of BT films can be recovered only by air-annealing at 800 and 900 °C. However, the vertical displacement represents the film/substrate pair strain which does not allow to perfectly match the butterfly form observed in piezoelectric ceramics for the thickness mode (d_{33}). Furthermore, as the BT layer is constrained in the transverse direction by the substrate, the vertical displacement is also influenced by the layer bending due to the transversal bending mode (d_{31}). Therefore, the S-E loops and the corresponding d_{33}^{*} values have been considered only for comparative analysis of different air-annealing conditions.

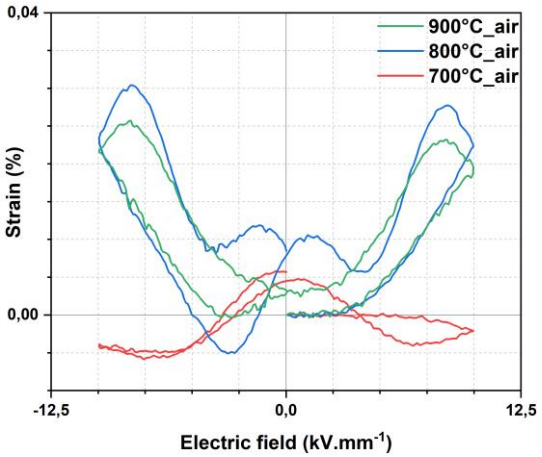

Figure 14. Strain-Electric field butterfly loops measured for air-annealed BT films (one-column, color online)

The reliability of the BT films after air-annealing at 900 °C was evaluated by electrical fatigue measurements (Fig. 15). The P-E loops show slight changes in shape and polarization values even after 10^6 fatigue cycles (Figure 15a). The P_r evolution (Fig 15.b) shows a slight decrease in P_r between 10^2 and 10^5 cycles. The minimum value observed after 10^5 cycles corresponds to approximately 88% of its initial value. These findings suggest that the BT film air-annealed at 900 °C demonstrates good electrical fatigue resistance, as evidenced by the stable P-E loops.

In ferroelectric films, electrical fatigue during bipolar switching cycles is commonly attributed to oxygen vacancies at the ferroelectric/electrode interface. Oxygen vacancies mobility under an electric field leads to their redistribution and ordering into defect planes, causing a hindrance to domain wall motion. This phenomenon, known as "domain pinning," has been extensively studied [56–58]. The number of pinned domain walls rises with the increasing electrical fatigue cycles and is also affected by spontaneous polarization of the ferroelectric material. Therefore, the good fatigue resistance (Figure 15a) confirms the significant effect of air annealing at 900 °C on the oxygen vacancies reduction. Despite this reduction, the slight decrease in remnant polarization indicates the presence of electrical fatigue. Several factors may contribute to this behavior, including residual oxygen vacancies remaining after air-annealing and potential mechanical damage such as microcracking caused by switching cycles and/or thermal treatment. Furthermore, metallic element diffusion from the substrate may contribute to oxygen vacancy formation and consequently promote electrical fatigue.

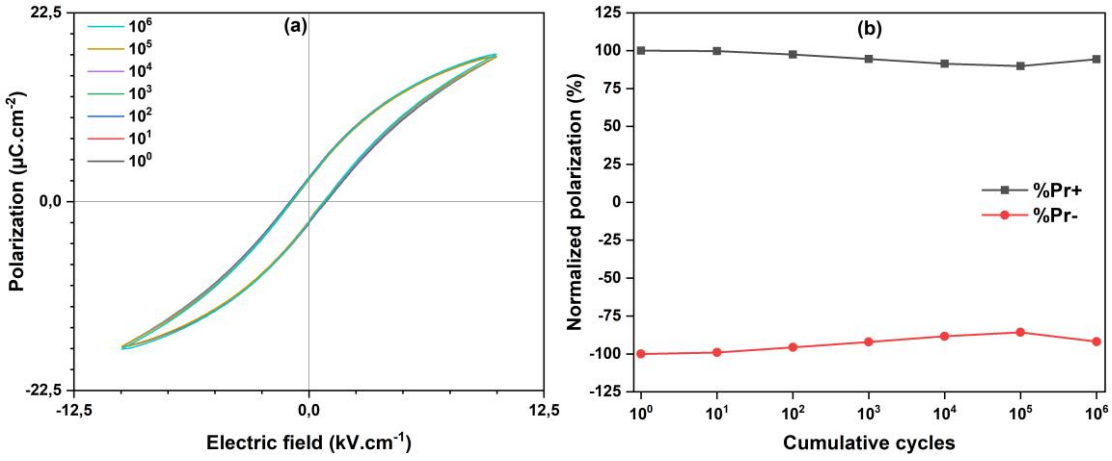

Figure 15. (a) Polarization-Electric field loops and (b) remnant polarization evolution for BT film annealed at 900 °C in air under 10^6 cumulative fatigue cycles (two-column, color online)

Figure 16 presents the leakage current density as a function of electric field (j-E) for the air-annealed BT films. Compared to the as-deposited film, the j-E curve for the film air-annealed at 700 °C exhibits a substantial reduction in leakage currents, with values not exceeding 0.1 µA.cm^{-2}, and electrical resistivity of the order of 10^{12} Ω.cm. Conversely, higher air-annealing temperatures (800 and 900 °C) lead to lower resistivity and higher leakage currents: the films air-annealed at 800 and 900 °C display higher leakage currents up to 3 µA.cm^{-2} and electrical resistivity up to 10^{10} Ω.cm only.

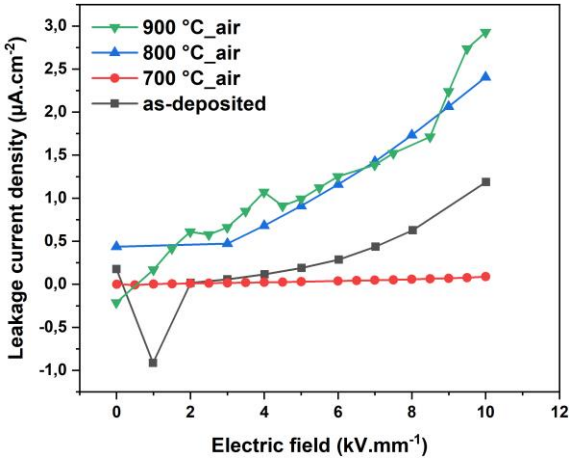

Figure 16. Leakage current density as function of electric field for as-deposited and air-annealed BT films (one-column, color online)

3.2.5. Summary of the results for air-annealed films:

To sum up, the obtained results for air annealing confirm the change in grain size and residual stress in BT film. The oxidization of the substrate as well as Fe, Co and Ni diffusion into BT annealed layers cannot be prevented. Thermal treatment at medium temperature (700 °C) is proved to be insufficient to restore the ferroelectricity of BT films, although it does improve their dielectric properties by releasing residual stress caused by the deposition mechanism. Grain growth occurs at higher temperatures (800 and 900 °C) and is necessary to obtain ferroelectric and piezoelectric properties. Thermal treatment in air results also in good fatigue resistance, as oxygen is incorporated within the material during annealing. To gain further insights into the behavior of AD films after thermal annealing, a comparison with films annealed under a low oxygen atmosphere content will be presented in the next section.

3.3. Annealing under argon flow:

3.3.1. Annealing parameters

The effect of argon-flow annealing on the substrate oxidation and the BT film characteristics was evaluated. By minimizing oxidation, we aimed also to protect the substrate, especially considering its relatively low thickness of 125 µm, which could be prone to deterioration at high annealing temperatures and dwell times. The studied temperatures for argon-annealing cycles were the same as those used for air-annealing.

As already observed for air-annealed films, Ar-annealed BT films conserved their cohesion with the kovar® substrates and showed no visible cracks. Film bending, typical of the AD process on thin substrates, is considerably reduced after annealing, resulting in relatively flat films. Interestingly, the 900 °C Ar-annealed BT film bends in the opposite direction compared to air-annealing, indicating tensile stress in the film.

3.3.2. Elemental interdiffusion analysis

EDS elemental analysis was performed to evaluate Fe, Ni, and Co diffusion within the BT films Ar-annealed at 800 °C (Fig. 17). It is important to note that interpretation of these EDS data are for comparative purpose only, since obtaining precise quantitative measurements would require more advanced analytical techniques. Although variable percentages of the three elements are detected, Fe is logically the predominant one in the film (~15 at.%), since iron presents the highest content in the kovar® substrate). This suggest diffusion of the elements of the metallic substrate (Fe/Ni/Co), even though the use of argon flow limits kovar® substrate oxidation during annealing.

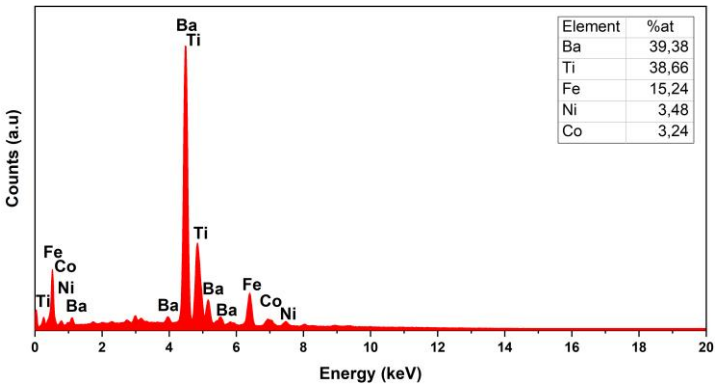

Figure 17. EDS elemental analysis results of a selected zone within the BT film argon-flow annealed at 800 °C (one-column, color online)

The evolution of iron content was evaluated in argon annealed BT films (Fig. 18), using the same conditions as for air annealing. A clear increase in Fe percentage is observed as we move away from the top surface of the film (from point A to point B). This confirms that Fe is more present at the film-substrate interface. Some differences can be noticed compared to BT film annealed in air. Indeed, the quasi-linear increase of Fe percentage is less regular for BT film annealed under argon flux, as some slight fluctuations can be observed at distances larger than 8 µm from top surface.

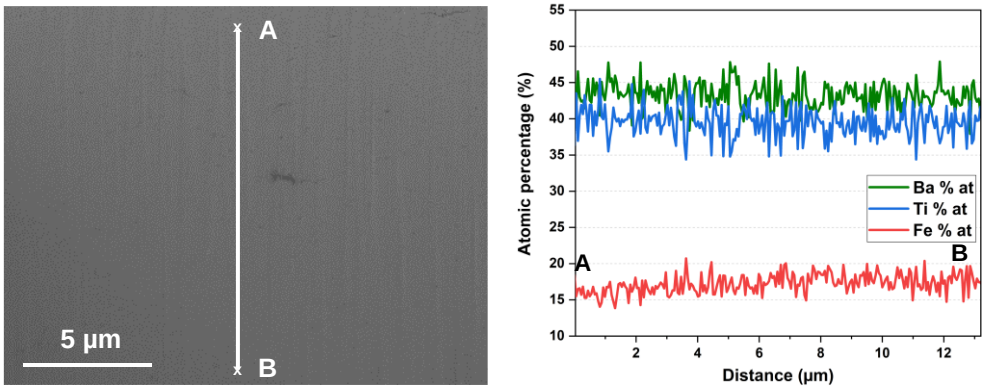

Figure 18. Chemical element profile line measured by EDS for argon-flow BT films at 800 °C (point B is close to the substate film interface and point A close to the top surface of the film) (one-column, color online)

3.3.3. Structural and microstructural analysis

Figure 19 presents the XRD patterns of the argon annealed films. Although metal oxide phase formation is significantly lower, the reduction in oxygen partial pressure by argon flow does not

totally prevent substrate oxidation. As for air-annealing, the XRD patterns show a crystallinity enhancement, evidenced by the reduction of the FWHM of XRD peaks and a significant increase in peak intensity.

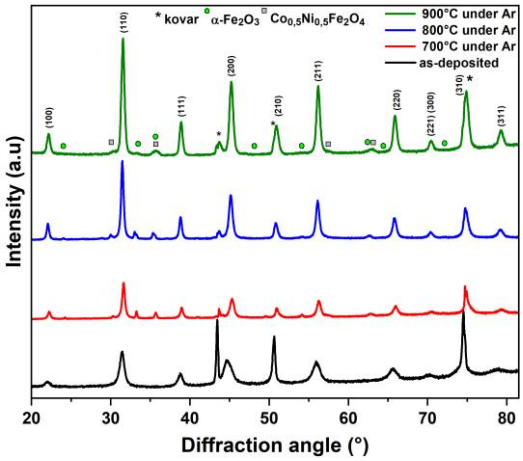

Figure 19. XRD patterns of argon-flow annealed BT films (one-column, color online)

Analysis of the XRD data for argon-annealed films by the Williamson-Hall method, similar to that performed on air-annealed films, are presented in Table 2. The results reveal an effect on grain size at 700 °C similar to the one observed for air annealing: the crystallite size is increased by annealing. However, the grain size is slightly larger here for 800 °C and increases significantly at 900 °C under argon compared to air annealing. This higher grain growth is associated with a better chemical diffusion due to the oxygen vacancies. Indeed, contrary to air-annealing, the lower oxygen content (Ar annealing) does not allow the suppression of the oxygen vacancies generated by fragmentation during the AD process.

On the other hand, as for air annealing, the microstrain is reduced compared to the as deposited film. The microstrain at 700 °C is slightly lower under argon compared to air atmosphere. However, the microstrain decreases only slightly at 800 °C compared to the significant decrease obtained for air-annealing (see Table 1). Furthermore, microstrain increases again at 900 °C, leading to a value (0.13) similar to the one obtained at 700 °C and larger than for air annealing. These results suggest that annealing under argon atmosphere at temperatures higher than 700 °C does not allow the same reduction of microstrain as for air annealing because it favors tensile stresses increasing with temperature.

Table 2. Crystallite size and microstrain analysis of BT films annealed under argon flow

Annealing temperature	Crystallite size (nm)	Microstrain (%)	Microstrain evolution (%)
As-deposited	26.2 ± 2.5	0.55 ± 0.11	0
700 °C	24.2 ± 2.0	0.12 ± 0.04	- 78
800 °C	36.3 ± 0.9	0.10 ± 0.02	- 82
900 °C	68.0 ± 0.7	0.13 ± 0.01	- 76

These microstrain changes were also analyzed using the shift of the Raman spectral bands (Fig. 20a). The results evidence that, after Ar-annealing, the Raman spectra of the films are closer to those of powder compared to air annealing. Indeed, a better definition is observed in the 270 cm^{-1} band, and the 305 cm^{-1} band become sharper at 800 and 900 °C. This Raman

band sharpening confirms the grain growth estimated by the Wiliamson-Hall method (WH). The WH estimations of the microstrain (Table 2) are also confirmed by the shift of the 515 cm^{-1} band, which initially decreases progressively from 700 °C to 800 °C but increases again at 900 °C (Fig. 20b). This stress increase is attributed to both low CTE of the substrate and the grain growth effect. Although grain growth is commonly associated with stress release in thin films under compressive stress, Chaudhari [59] has reported a dual effect of stress generation and stress release. This statement explains the anomalous increase in tensile stress in BT films argon-flow annealed at 900 °C.

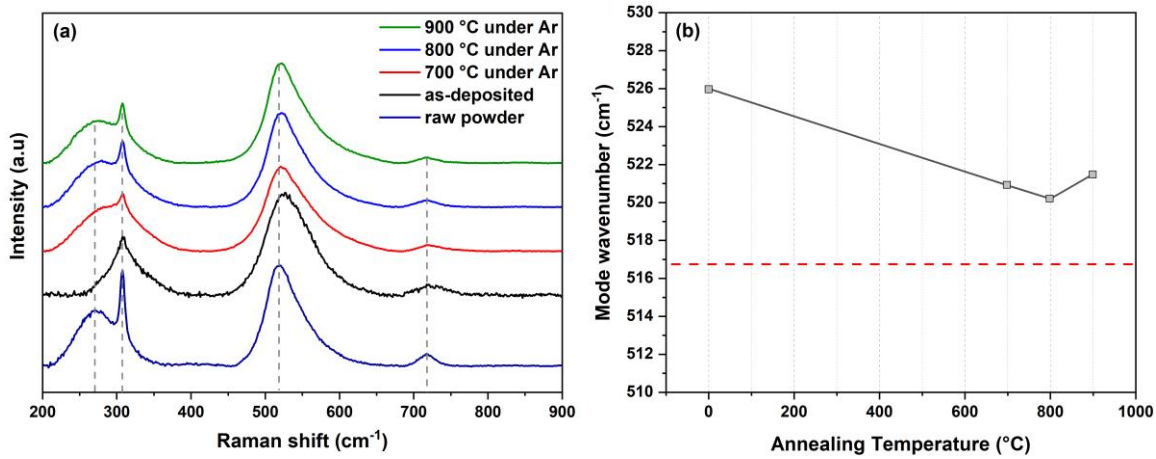

Figure 20. (a) Raman spectra of argon-flow annealed BT films and (b) 515 cm^{-1} Raman mode shift (two-column, color online)

3.3.4. Electrical properties

Figure 21 presents the P-E loops measured for Ar-annealed films. For 700 °C, the film displays a linear dielectric-type behavior with a higher slope (higher permittivity) than for the as-deposited BT films. No clear indication of polarization switching or P-E curve saturation is observed. On the other hand, 800 °C Ar-annealed BT film clearly exhibits a ferroelectric behavior, with remnant polarization of 5.6 µC.cm^{-2}, similar to those obtained for air-annealing (5.7 µC.cm^{-2}). An increase in annealing temperature from 800 to 900 °C leads to a slightly more opened P-E curve, which also shows a ferroelectric behavior. However, saturation polarization P_s decreases from 17.2 µC.cm^{-2} to 14.8 µC.cm^{-2}, while the remnant polarization P_r increases slightly to 6.6 µC.cm^{-2}.

Since no grain growth activation is evidenced at 700 °C, the slight improvement in polarization for the 700 °C Ar-annealed film is attributed to stress release, as demonstrated hereabove by XRD and Raman analysis. The increase in remnant polarization at 800 and 900 °C can be explained by a combination of the enhanced grain growth and the residual tensile stress. Indeed, the previous results from literature on $BaTiO_3$ thick films demonstrated that compressive stress generally lead to lowered dielectric properties [37]. In contrast, slight tensile stress generated for BT films on YSZ substrates resulted in better properties [31].

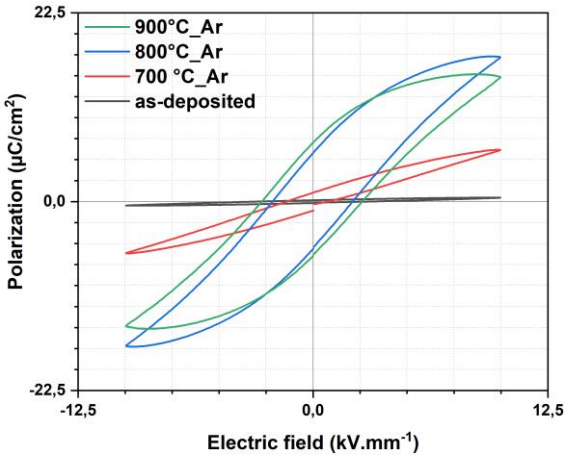

Figure 21. Polarization-Electric field loops of argon-flow annealed BT films (one-column, color online)

Figure 22 displays the Strain-Electric field (S-E) butterfly loops measured for the Ar-annealed films. The film annealed at 700 °C exhibits an irregular S-E curve with low strain. Increasing the annealing temperature results in an increase in strain. The films annealed at 800 and 900 °C achieve maximal strains of 0.025% and 0.04%, respectively. At 800 °C, the S-E curve shows a more pronounced butterfly-like shape compared to the one obtained at 900 °C. These measurements confirm the recovery of piezoelectricity for 800 and 900 °C annealed BT film. The higher strain values observed for the 900 °C annealed film can be attributed to the enhanced grain growth and tensile stress demonstrated hereabove by XRD and Raman spectroscopy.

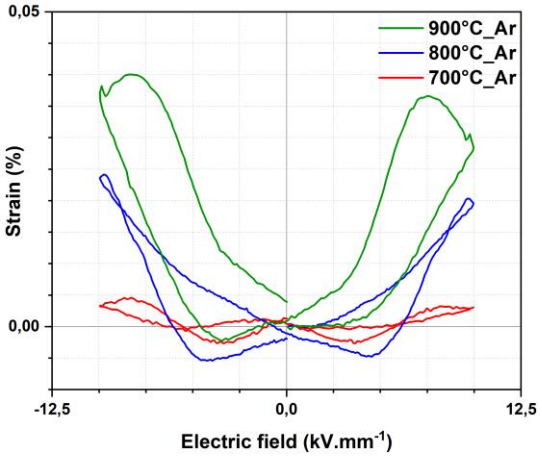

Figure 22. Strain-Electric field butterfly loops of argon-flow annealed BT films (one-column, color online)

Fatigue measurements performed on the 900 °C Ar-annealed BT film are summarized in Figure 23 (same parameters as for those air-annealed). The results show that the P-E loops remain stable during 10^3 fatigue cycles. However, both maximum polarization (P_{max}) and remnant polarization (P_r) gradually decrease with increasing cumulative pulse cycles. Compared to the 800 °C air-annealed sample, the polarization decrease is more pronounced, with the lowest polarization after 10^6 cycles representing 75% of the initial value. The increased fatigue of Ar-annealed films is attributed to the higher content of oxygen vacancies. Indeed, annealing under a low oxygen content favors the formation of oxygen vacancies. During the fatigue process, the repeated application of electric fields can induce the movement of these vacancies, altering the kinetics of polarization switching [56–58]. The high density of oxygen defects acting as trapping sites for electric charges hinders the motion of domain walls, leading

to increased fatigue. Hence, the effect of annealing in a low oxygen content on the formation of new oxygen vacancies is confirmed. Mechanical stress, as evidenced by XRD and Raman analysis, can on the other hand contribute to increased fatigue through the potential formation of microcracks or other structural defects, which facilitate the pinning of domain walls and intensify fatigue phenomenon [60,61].

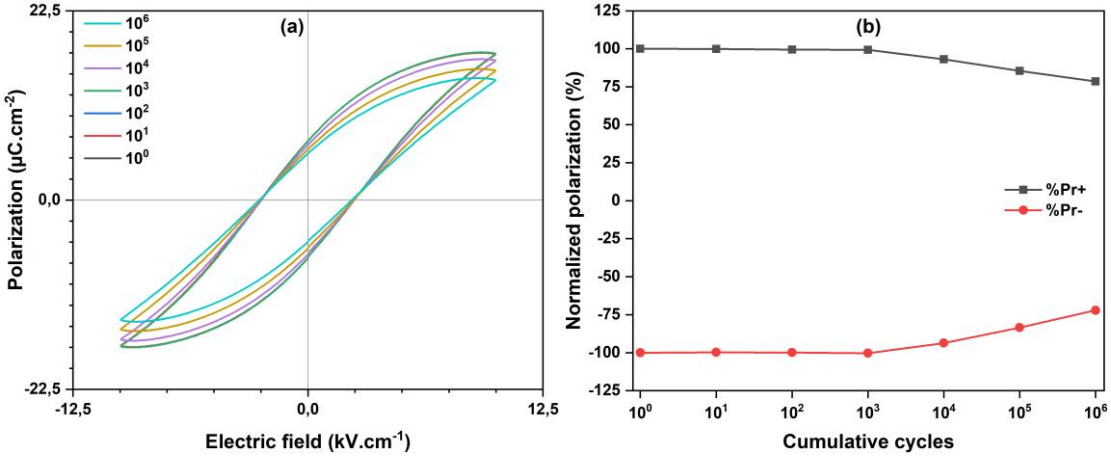

Figure 23. (a) Polarization-Electric field loops and (b) remnant polarization evolution for 900°C argon-annealed BT film (two-column, color online)

Figure 24 displays the j-E curves measured for argon annealed films. The leakage current density in the 700 °C Ar-annealed film is of the order of 1 μA.cm^{-2} for an electric field of 10 kV.mm^{-1}. However, the leakage current density value increases to 4 and 10 μA.cm^{-2} with increasing annealing temperature to 800 and 900 °C, respectively. As a consequence, the electrical resistivity of film annealed at 700 °C is ~10^{10} Ω.cm, while it decreases to ~10^{9} Ω.cm for those annealed at 800 and 900 °C. These results indicate a modest effect on leakage current and electrical resistivity for the 700 °C annealed film, while they are deteriorated magnitude for films annealed at 800 and 900 °C.

These observations align with the findings from measurements on films annealed in air atmosphere, wherein annealing at 700 °C yields more favorable results compared to 800 and 900 °C. The most probable explanation for this results is the higher level of diffusion of metallic elements at higher temperatures (800 and 900 °C) compared to 700 °C as well as higher oxygen vacancies concentration. However, it is important to note that, in contrast to films annealed in air, the improvement observed in electrical resistivity is not observed when annealing under argon. This suggests that annealing under argon atmosphere may not be the optimal approach for enhancing the dielectric characteristics of the films.

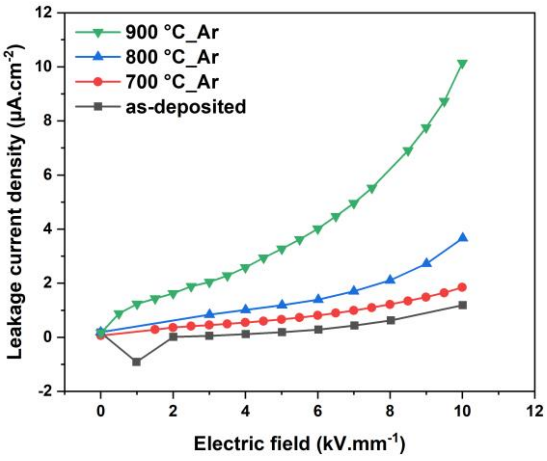

Figure 24. Leakage current density as function of electric field for argon-annealed BT films (one-column, color online)

4. Comparative discussion of annealing conditions

Figure 25 summarizes the evolution of crystallite size and microstrain with temperature for both air and argon annealed BT films. Comparative analysis of the results reveals distinct effects on the microstructural evolution and hence on properties of annealed BT films. In both cases, stress release is evidenced, especially at low annealing temperatures, leading mainly to an increased polarization. The stress release observed for the low temperature part (T < 700°C) aligns well with previous studies performed on freestanding films, which evidenced relaxation of stress for temperatures lower than 500 °C, mainly attributed to a change in the defect structure (mainly oxygen vacancies) [38,62].

Grain growth and piezo/ferroelectric behavior recovery are possible only at higher temperatures (≥ 800 °C) regardless of the annealing atmosphere. However, the higher grain growth in Ar-annealed films above 700 °C promotes a concurrent increase in residual tensile stress, especially at 900 °C. Differences emerge also for fatigue resistance, with argon-annealed films displaying increased fatigue, possibly due to the creation of oxygen vacancies under low-oxygen conditions. Conversely, air-annealed films exhibit good fatigue resistance, suggesting a reduction in oxygen vacancies.

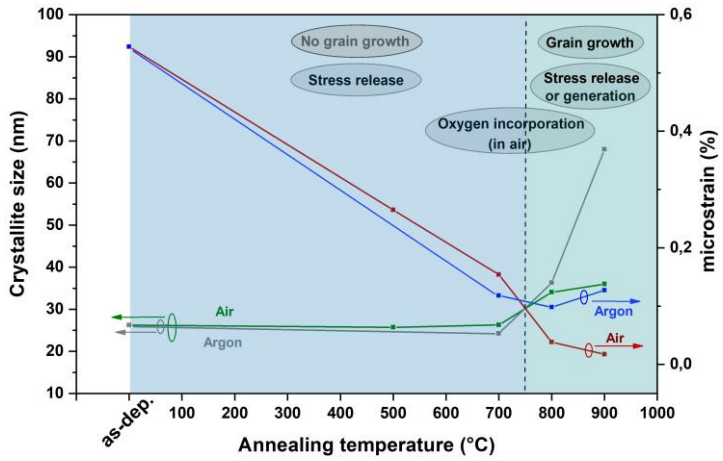

Figure 25. Evolution of crystallite size and microstrain of air and argon-flow annealed BT films (one-column, color online)

Leakage currents and electrical resistivity present another distinguishing feature (Table 3). Air-annealing at 700 °C demonstrates a significant leakage current reduction correlated to a notable increase in electrical resistivity. Conversely, argon-annealing does not exhibit the same level of improvement in electrical resistivity. This divergence suggests that the low oxygen content during argon annealing may not be as effective in reducing the density of oxygen defect and thus does not improve the resistivity values. Remarkably, the leakage current density for 700 °C air-annealed BT films (0.07 $\mu A.cm^{-2}$= $0.7x10^{-7}$ $A.cm^{-2}$) meets the general criteria required for ceramic capacitors (<10^{-7} $A.cm^{-2}$) [34,63]. This result is consistent with those reported by Imanaka et al. for a 1 µm-thick $BaTiO_3$ film deposited on copper, which exhibited a current density below 10^{-7} $A.cm^{-2}$ under 10 V [34]. Nonetheless, given that dielectric breakdown is not reached at 10 $kV.mm^{-1}$, complementary experiments at higher electric fields are needed to precisely determine the dielectric strength of this interesting BT film.

Table 3. Summary of electrical resistivity and leakage current density for annealed BT films

Annealing Temperature (°C)	Atmosphere	Resistivity (Ω.cm)	J_{max}(μA.cm^{-2})
As-deposited	–	6.5x10^{9}	1.12
700	Air	1.2x10^{12}	0.07
800		2.3x10^{10}	2.40
900		3.3x10^{10}	2.92
700	Argon-flow	4.2x10^{10}	1.84
800		2.1x10^{9}	3.66
900		7.4x10^{9}	10.14

Table 4 provides a summary of the P_r values reported in this paper with respect to those of previous studies for several different substrates. The remnant polarization (P_r) values obtained in this study are significantly higher than those reported in $BaTiO_3$ thick films deposited by Aerosol Deposition (AD) method on other substrates. Typically, the best ferroelectric properties have been reported in BT films deposited on ceramic substrates, which is essentially attributed to their Coefficient of Thermal Expansion (CTE) comparable to that of $BaTiO_3$ material. With a low CTE mismatch, residual compressive stress is minimized, and in some cases, weak tensile stress is induced after thermal annealing. For instance, a P_r value of 4 μC.cm^{-2} was obtained using a YSZ substrate [31], which has a slightly lower CTE (10.0x10^{-6} K^{-1} [64]) than $BaTiO_3$ (14.7x10^{-6} K^{-1} [64]). This leads to a weak tensile stress after thermal treatment, thereby enhancing the ferroelectric/piezoelectric properties of BT films.

Conversely, when the CTE of the substrate exceeds that of $BaTiO_3$, as in the case of metallic substrates, compressive stress is observed, leading to lower properties. Prior studies focusing on low-temperature annealing have highlighted the negative effect of compressive stress in as-deposited BT films on their dielectric and ferroelectric properties. Using synchrotron X-Ray microdiffraction, Khansur et al. have measured a biaxial compressive stress of -672 MPa in as-deposited BT films. This stress was reduced to -271 MPa through annealing at 500 °C, resulting in enhanced dielectric and ferroelectric responses [33,65]. Another study by Bentzen et al. confirmed stress release in low-temperature annealed BT films, mainly observed in the 400-550 °C range. However, higher temperatures led to an apparent re-introduction of stress, resulting in a reduction in polarization values compared to 550 °C annealed film, which exhibited the highest polarization values, even though annealing at > 650 °C resulted in an enhanced hysteresis [39]. On the other side, a study conducted by Maruyama et al. on BT films with varying thicknesses reported a difference in thermal compressive stress depending on film thickness. Thicker BT films (30 μm) exhibited lower stress and facilitated polarization switching compared to thinner ones (10-20 μm). This difference was explained by thermal compressive stress affecting the mobility of the domains in the grains and influencing the values of coercive field E_c [66]. This tendency does not match with the result observed for PZT thick films, where enhanced properties were observed with compressive residual stress [67]. This discrepancy in behavior between $BaTiO_3$ and PZT could be attributed to the difference in material characteristics and stress response.

Kovar®, as a low CTE metallic substrate, was chosen in this study to improve the ferro/piezoelectric properties of annealed BT films by controlling residual stress between BT films and kovar® substrates. For instance, the high remnant polarization of 6.63 μC.cm^{-2} obtained for 900 °C Ar-annealed BT film surpasses those reported in the literature for BT films

deposited on both metallic and ceramic substrates. Remarkably, it even exceeds that observed for a stress-free, free-standing BT film annealed at a higher temperature of 1000 °C (> 900 °C) [36]. As already specified in our introduction, weak tensile stress has been shown to result in better ferro/piezoelectric properties [31,37]. The achieved ferro/piezoelectric responses in our study, notably the high P_r value, confirm that relatively higher tensile stress can further improve the ferro/piezoelectric properties compared to weak tensile stress created with ceramic substrates such as YSZ. Hence, it is demonstrated that, in addition to high temperature induced grain growth, the control of residual tensile stress is a promising way to enhance the ferroelectric/piezoelectric properties of AD-fabricated BT films and hence it is demonstrated as a promising way to improve the ferroelectric/piezoelectric properties of AD-fabricated BT films.

Table 4. Comparison of P_r values from this study with those reported in the literature for $BaTiO_3$ thick films deposited by AD on different substrates

Substrate	Annealing temperature (°C)	Applied electric field ($kV.mm^{-1}$)	Remanent polarization ($\mu C.cm^{-2}$)	Reference
kovar®	900 (Ar-flow)	10	6.6	This study
kovar®	900 (Air)	10	2.6	This study
304SUS	750	50	~2.5	[39]
SUS	1200	10	~2.4	[37]
SUS	1100	5	~2.2	[66]
YSZ	1100	10	4	[31]
Free-standing	1000	6.5	~5	[36]

4. Conclusions

$BaTiO_3$ thick films were successfully deposited on kovar® substrates by Aerosol Deposition (AD) method. The tetragonal perovskite symmetry of $BaTiO_3$ was conserved in the deposited films, as confirmed by Raman spectroscopy analysis. Initially, the as-deposited $BaTiO_3$ films did not exhibit any ferroelectric behavior, owing to the particle fragmentation into 5-25 nm sized crystallites (size effect) during deposition. Post-annealing at temperatures below 800 °C primarily affected the residual stress within the $BaTiO_3$ films rather than promoting grain growth. Increasing the annealing temperature to 800 °C and especially to 900 °C led to significant grain growth in the $BaTiO_3$ films, which favored the recovery of their ferroelectric and piezoelectric properties. The 900 °C argon-flow annealed $BaTiO_3$ film exhibited the highest ferroelectric/piezoelectric response, with a remnant polarization of ~6.6 $\mu C.cm^{-2}$ and a maximum strain of 0.04 %. However, the increase in oxygen vacancies during annealing in a low oxygen partial pressure (argon annealing) induced a lower fatigue resistance compared to the 900 °C air-annealed BT film. Moreover, the measurement of leakage currents showed a decrease at relatively low temperatures (700 °C) for air-annealed films. Conversely, an increase in leakage currents associated with a decrease in electrical resistivity was observed at higher temperatures independently on the annealing atmosphere (800 and 900 °C).

Findings in this paper suggest that low-temperature annealing is optimal for AD-produced $BaTiO_3$ films intended for dielectric applications, as it effectively improves relative permittivity,

electrical resistivity and reduces leakage currents. However, for ferroelectric and piezoelectric applications, higher annealing temperatures are required. The choice of annealing atmosphere should be tailored to specific performance requirements; air-annealing offering better fatigue resistance, while argon-flow annealing leads to better ferroelectric/piezoelectric responses.

Declaration of competing interest

The authors declare that they have no financial interests or personal relationships that could have influenced the work reported in this paper.

Acknowledgments

This work is supported by the Nouvelle Aquitaine Region [project AAPR 2021A-2020-12121010] which partially funds Anass Chrir's PhD thesis.

Anass Chrir also benefited from an institutional grant from the National Research Agency under the investments for the future program with reference ANR-18-EURE-0017 TACTIC.

References

[1] A. Toprak, O. Tigli, Piezoelectric energy harvesting: State-of-the-art and challenges, Appl. Phys. Rev. 1 (2014) 031104. https://doi.org/10.1063/1.4896166.

[2] D.B. Deutz, N.T. Mascarenhas, J.B.J. Schelen, D.M. de Leeuw, S. van der Zwaag, P. Groen, Flexible Piezoelectric Touch Sensor by Alignment of Lead-Free Alkaline Niobate Microcubes in PDMS, Adv. Funct. Mater. 27 (2017) 1700728. https://doi.org/10.1002/adfm.201700728.

[3] W. Zhang, G. Meng, H. Li, Adaptive vibration control of micro-cantilever beam with piezoelectric actuator in MEMS, Int. J. Adv. Manuf. Technol. 28 (2006) 321–327. https://doi.org/10.1007/s00170-004-2363-5.

[4] J. Bernard, Piezoelectric transducers using lead titanate and lead zirconate, US2708244A, 1955.

[5] Directive 2002/95/EC on the restriction of the use of certain hazardous substances in electrical and electronic equipment, Official Journal of the European Union, L37/19-L37/23, 2003, n.d.

[6] Directive 2002/96/EC on waste electrical and electronic equipment (WEEE), Official Journal of the European Union, L37/24-L37/3, 2003, n.d.

[7] T. Karaki, K. Yan, T. Miyamoto, M. Adachi, Lead-Free Piezoelectric Ceramics with Large Dielectric and Piezoelectric Constants Manufactured from $BaTiO_3$ Nano-Powder, Jpn. J. Appl. Phys. 46 (2007) L97. https://doi.org/10.1143/JJAP.46.L97.

[8] W. Liu, X. Ren, Large Piezoelectric Effect in Pb-Free Ceramics, Phys. Rev. Lett. 103 (2009) 257602. https://doi.org/10.1103/PhysRevLett.103.257602.

[9] Y. Saito, H. Takao, T. Tani, T. Nonoyama, K. Takatori, T. Homma, T. Nagaya, M. Nakamura, Lead-free piezoceramics, Nature 432 (2004) 84–87. https://doi.org/10.1038/nature03028.

[10] J. Akedo, M. Ichiki, K. Kikuchi, R. Maeda, Jet molding system for realization of three-dimensional micro-structures, Sens. Actuators Phys. 69 (1998) 106–112. https://doi.org/10.1016/S0924-4247(98)00059-4.

[11] J. Akedo, M. Lebedev, Microstructure and Electrical Properties of Lead Zirconate Titanate ($Pb(Zr_{52}/Ti_{48})O_3$) Thick Films Deposited by Aerosol Deposition Method, Jpn. J. Appl. Phys. 38 (1999) 5397. https://doi.org/10.1143/JJAP.38.5397.

[12] J. Akedo, Masaakiichiki, R. Maeda, New functional ceramic deposition method for MEMS, Ferroelectrics 224 (1999) 331–337. https://doi.org/10.1080/00150199908210584.

[13] J. Akedo, Room Temperature Impact Consolidation (RTIC) of Fine Ceramic Powder by Aerosol Deposition Method and Applications to Microdevices, J. Therm. Spray Technol. 17 (2008) 181–198. https://doi.org/10.1007/s11666-008-9163-7.

[14] J. Akedo, M. Lebedev, Piezoelectric properties and poling effect of $Pb(Zr,Ti)O_3$ thick films prepared for microactuators by aerosol deposition, Appl. Phys. Lett. 77 (2000) 1710–1712. https://doi.org/10.1063/1.1309029.

[15] S.-M. Nam, N. Mori, H. Kakemoto, S. Wada, J. Akedo, T. Tsurumi, Alumina Thick Films as Integral Substrates Using Aerosol Deposition Method, Jpn. J. Appl. Phys. 43 (2004) 5414. https://doi.org/10.1143/JJAP.43.5414.

[16] M. Isaza-Ruiz, J. Henon, O. Durand-Panteix, G. Etchegoyen, F. Rossignol, P. Marchet, Elaboration of lead-free $Na_{0.5}Bi_{0.5}TiO_3$–$BaTiO_3$ (NBT-BT) thick films by aerosol deposition method (ADM), Ceram. Int. 42 (2016) 14635–14641. https://doi.org/10.1016/j.ceramint.2016.06.084.

[17] J.-J. Choi, J.-H. Choi, J. Ryu, B.-D. Hahn, J.-W. Kim, C.-W. Ahn, W.-H. Yoon, D.-S. Park, Microstructural evolution of YSZ electrolyte aerosol-deposited on porous NiO-YSZ, J. Eur. Ceram. Soc. 32 (2012) 3249–3254. https://doi.org/10.1016/j.jeurceramsoc.2012.04.024.

[18] A. Iwata, J. Akedo, Hexagonal to cubic crystal structure transformation during aerosol deposition of aluminum nitride, J. Cryst. Growth 275 (2005) e1269–e1273. https://doi.org/10.1016/j.jcrysgro.2004.11.082.

[19] G.-S. Ham, S.-H. Kim, J.-Y. Park, K.-A. Lee, High Temperature Oxidation Property of SiC Coating Layer Fabricated by Aerosol Deposition Process, Arch. Metall. Mater. 62 (2017). https://doi.org/10.1515/amm-2017-0206.

[20] S. Kauffmann-Weiss, W. Hässler, E. Guenther, J. Scheiter, S. Denneler, P. Glosse, T. Berthold, M. Oomen, T. Arndt, T. Stöcker, D. Hanft, R. Moos, M. Weiss, F. Weis, B. Holzapfel, Superconducting Properties of Thick Films on Hastelloy Prepared by the Aerosol Deposition Method With Ex Situ MgB_2 Powder, IEEE Trans. Appl. Supercond. 27 (2017) 1–4. https://doi.org/10.1109/TASC.2017.2669479.

[21] M.A. Piechowiak, J. Henon, O. Durand-Panteix, G. Etchegoyen, V. Coudert, P. Marchet, F. Rossignol, Growth of dense Ti_3SiC_2 MAX phase films elaborated at room temperature by aerosol

deposition method, J. Eur. Ceram. Soc. 34 (2014) 1063–1072. https://doi.org/10.1016/j.jeurceramsoc.2013.11.019.
[22] J. Henon, M.A. Piechowiak, O. Durand-Panteix, G. Etchegoyen, O. Masson, C. Dublanche-Tixier, P. Marchet, B. Lucas, F. Rossignol, Dense and highly textured coatings obtained by aerosol deposition method from Ti_3SiC_2 powder: Comparison to a dense material sintered by Spark Plasma Sintering, J. Eur. Ceram. Soc. 35 (2015) 1179–1189. https://doi.org/10.1016/j.jeurceramsoc.2014.10.012.
[23] J.-J. Choi, S.-H. Oh, H.-S. Noh, H.-R. Kim, J.-W. Son, D.-S. Park, J.-H. Choi, J. Ryu, B.-D. Hahn, W.-H. Yoon, H.-W. Lee, Low temperature fabrication of nano-structured porous LSM–YSZ composite cathode film by aerosol deposition, J. Alloys Compd. 509 (2011) 2627–2630. https://doi.org/10.1016/j.jallcom.2010.11.169.
[24] H.-J. Kim, Y.-H. Kim, J.-W. Lee, S.-M. Nam, Y.J. Yoon, J.-H. Kim, Residual Stress Relief in Al_2O_3-Poly-Tetra-Fluoro-Ethylene Hybrid Thick Films for Integrated Substrates Using Aerosol Deposition, J. Nanoelectron. Optoelectron. 7 (2012) 287–291. https://doi.org/10.1166/jno.2012.1305.
[25] Fabrication of TiO_2/Cu hybrid composite films with near zero TCR and high adhesive strength via aerosol deposition - ScienceDirect, Ceram. Int. 44 (2018) 18736–18742. https://doi.org/10.1016/j.ceramint.2018.07.103.
[26] Y.-Y. Wang, Y. Liu, C.-J. Li, G.-J. Yang, J.-J. Feng, K. Kusumoto, Investigation on the Electrical Properties of Vacuum Cold Sprayed SiC-$MoSi_2$ Coatings at Elevated Temperatures, J. Therm. Spray Technol. 20 (2011) 892–897. https://doi.org/10.1007/s11666-011-9635-z.
[27] T. Tsurumi, J. Ma, J. Li, H. Kakemoto, D. Tsukiori, R. Sakamaki, S. Wada, J. Akedo, Aerosol deposition for ceramic thick film formation at room temperature, in: 2007 Sixt. IEEE Int. Symp. Appl. Ferroelectr., 2007: pp. 464–465. https://doi.org/10.1109/ISAF.2007.4393299.
[28] K. Mihara, T. Hoshina, H. Takeda, T. Tsurumi, Controlling factors of film-thickness in improved aerosol deposition method, J. Ceram. Soc. Jpn. 117 (2009) 868–872. https://doi.org/10.2109/jcersj2.117.868.
[29] M. Suzuki, J. Akedo, Temperature Dependence of Dielectric Properties of Barium Titanate Ceramic Films Prepared by Aerosol Deposition Method, Jpn. J. Appl. Phys. 49 (2010) 09MA10. https://doi.org/10.1143/JJAP.49.09MA10.
[30] J.-M. Oh, S.-M. Nam, Thickness limit of $BaTiO_3$ thin film capacitors grown on SUS substrates using aerosol deposition method, Thin Solid Films 518 (2010) 6531–6536. https://doi.org/10.1016/j.tsf.2010.03.159.
[31] J.-H. Park, Y. Kawakami, M. Suzuki, J. Akedo, Fabrication and Characterization of Optical Micro-Electro-Mechanical System Scanning Devices Using $BaTiO_3$-Based Lead-Free Piezoelectric-Coated Substrate Sheet by Aerosol Deposition, Jpn. J. Appl. Phys. 50 (2011) 09ND19. https://doi.org/10.1143/JJAP.50.09ND19.
[32] T. Furuta, S. Hatta, Y. Kigoshi, T. Hoshina, H. Takeda, T. Tsurumi, Dielectric Properties of Nanograined $BaTiO_3$ Ceramics Fabricated by Aerosol Deposition Method, Key Eng. Mater. 485 (2011) 183–186. https://doi.org/10.4028/www.scientific.net/kem.485.183.
[33] N.H. Khansur, U. Eckstein, L. Benker, U. Deisinger, B. Merle, K.G. Webber, Room temperature deposition of functional ceramic films on low-cost metal substrate, Ceram. Int. 44 (2018) 16295–16301. https://doi.org/10.1016/j.ceramint.2018.06.027.
[34] Y. Imanaka, N. Hayashi, M. Takenouchi, J. Akedo, Aerosol deposition for post-LTCC, J. Eur. Ceram. Soc. 27 (2007) 2789–2795. https://doi.org/10.1016/j.jeurceramsoc.2006.11.055.
[35] C.E. Folgar, C. Suchicital, S. Priya, Solution-based aerosol deposition process for synthesis of multilayer structures, Mater. Lett. 65 (2011) 1302–1307. https://doi.org/10.1016/j.matlet.2011.01.069.
[36] T. Hoshina, T. Furuta, Y. Kigoshi, S. Hatta, N. Horiuchi, H. Takeda, T. Tsurumi, Size Effect of Nanograined $BaTiO_3$ Ceramics Fabricated by Aerosol Deposition Method, Jpn. J. Appl. Phys. 49 (2010) 09MC02. https://doi.org/10.1143/JJAP.49.09MC02.
[37] Y. Kawakami, M. Watanabe, K.-I. Arai, S. Sugimoto, Piezoelectric Properties and Microstructure of $BaTiO_3$ Films on Heat-Resistant Stainless-Steel Substrates Deposited Using Aerosol Deposition, Trans. Mater. Res. Soc. Jpn. 41 (2016) 279–283. https://doi.org/10.14723/tmrsj.41.279.
[38] U. Eckstein, N.H. Khansur, M. Bergler, D. Urushihara, T. Asaka, K. Kakimoto, M. Sadl, M. Dragomir, H. Uršič, D. de Ligny, K.G. Webber, Room temperature deposition of freestanding $BaTiO_3$ films: temperature-induced irreversible structural and chemical relaxation, J. Mater. Sci. 57 (2022) 13264–13286. https://doi.org/10.1007/s10853-022-07467-3.

[39] M. Bentzen, J. Maier, U. Eckstein, J. He, A. Henss, N. Khansur, J. Glaum, Enhanced grain growth and dielectric properties in aerosol deposited $BaTiO_3$, J. Eur. Ceram. Soc. 43 (2023) 4386–4394. https://doi.org/10.1016/j.jeurceramsoc.2023.03.012.
[40] G.-T. Hwang, V. Annapureddy, J.H. Han, D.J. Joe, C. Baek, D.Y. Park, D.H. Kim, J.H. Park, C.K. Jeong, K.-I. Park, J.-J. Choi, D.K. Kim, J. Ryu, K.J. Lee, Self-Powered Wireless Sensor Node Enabled by an Aerosol-Deposited PZT Flexible Energy Harvester, Adv. Energy Mater. 6 (2016) 1600237. https://doi.org/10.1002/aenm.201600237.
[41] U. Eckstein, J. Exner, A. Bencan Golob, K. Ziberna, G. Drazic, H. Ursic, H. Wittkämper, C. Papp, J. Kita, R. Moos, K.G. Webber, N.H. Khansur, Temperature-dependent dielectric anomalies in powder aerosol deposited ferroelectric ceramic films, J. Materiomics 8 (2022) 1239–1250. https://doi.org/10.1016/j.jmat.2022.05.001.
[42] C.A. Schneider, W.S. Rasband, K.W. Eliceiri, NIH Image to ImageJ: 25 years of image analysis, Nat. Methods 9 (2012) 671–675. https://doi.org/10.1038/nmeth.2089.
[43] J. Akedo, S. Nakano, J. Park, S. Baba, K. Ashida, The aerosol deposition method For production of high performance micro devices with low cost and low energy consumption, Synth. Engl. Ed. 1 (2008) 121–130. https://doi.org/10.5571/syntheng.1.121.
[44] D.-W. Lee, S.-M. Nam, Factors affecting surface roughness of Al_2O_3 films deposited on Cu substrates by an aerosol deposition method, J. Ceram. Process. Res. 11 (2010) 100–106.
[45] M. El Marssi, F. Le Marrec, I.A. Lukyanchuk, M.G. Karkut, Ferroelectric transition in an epitaxial barium titanate thin film: Raman spectroscopy and x-ray diffraction study, J. Appl. Phys. 94 (2003) 3307–3312. https://doi.org/10.1063/1.1596720.
[46] M. DiDomenico, S.H. Wemple, S.P.S. Porto, R.P. Bauman, Raman Spectrum of Single-Domain $BaTiO_3$, Phys. Rev. 174 (1968) 522–530. https://doi.org/10.1103/PhysRev.174.522.
[47] M.B. Smith, K. Page, T. Siegrist, P.L. Redmond, E.C. Walter, R. Seshadri, L.E. Brus, M.L. Steigerwald, Crystal Structure and the Paraelectric-to-Ferroelectric Phase Transition of Nanoscale $BaTiO_3$, J. Am. Chem. Soc. 130 (2008) 6955–6963. https://doi.org/doi/10.1021/ja0758436.
[48] R. Naik, J.J. Nazarko, C.S. Flattery, U.D. Venkateswaran, V.M. Naik, M.S. Mohammed, G.W. Auner, J.V. Mantese, N.W. Schubring, A.L. Micheli, A.B. Catalan, Temperature dependence of the Raman spectra of polycrystalline $Ba_{1-x}Si_xTiO_3$, Phys. Rev. B 61 (2000) 11367–11372. https://doi.org/10.1103/PhysRevB.61.11367.
[49] T. Sakashita, M. Deluca, S. Yamamoto, H. Chazono, G. Pezzotti, Stress dependence of the Raman spectrum of polycrystalline barium titanate in presence of localized domain texture, J. Appl. Phys. 101 (2007) 123517. https://doi.org/10.1063/1.2747217.
[50] M. Nakada, K. Ohashi, J. Akedo, Electro-Optical Properties and Structures of (Pb, La)(Zr, Ti)O_3 and $PbTiO_3$ Films Prepared Using Aerosol Deposition Method, Jpn. J. Appl. Phys. 43 (2004) 6543. https://doi.org/10.1143/JJAP.43.6543.
[51] T. Hoshina, H. Kakemoto, T. Tsurumi, S. Wada, M. Yashima, Size and temperature induced phase transition behaviors of barium titanate nanoparticles, J. Appl. Phys. 99 (2006) 054311. https://doi.org/10.1063/1.2179971.
[52] T. Hoshina, Size effect of barium titanate: fine particles and ceramics, J. Ceram. Soc. Jpn. 121 (2013) 156–161. https://doi.org/10.2109/jcersj2.121.156.
[53] K. Nadaud, M. Sadl, M. Bah, F. Levassort, H. Ursic, Effect of thermal annealing on dielectric and ferroelectric properties of aerosol-deposited $0.65Pb(Mg_{1/3}Nb_{2/3})O_3$-$0.35PbTiO_3$ thick films, Appl. Phys. Lett. 120 (2022) 112902. https://doi.org/10.1063/5.0087389.
[54] Z. Yao, C. Wang, Y. Li, H.-K. Kim, N.-Y. Kim, Effects of starting powder and thermal treatment on the aerosol deposited $BaTiO_3$ thin films toward less leakage currents, Nanoscale Res. Lett. 9 (2014) 435. https://doi.org/10.1186/1556-276X-9-435.
[55] S. Shao, J. Zhang, Z. Zhang, P. Zheng, M. Zhao, J. Li, C. Wang, High piezoelectric properties and domain configuration in $BaTiO_3$ ceramics obtained through the solid-state reaction route, J. Phys. Appl. Phys. 41 (2008) 125408. https://doi.org/10.1088/0022-3727/41/12/125408.
[56] U. Robels, G. Arlt, Domain wall clamping in ferroelectrics by orientation of defects, J. Appl. Phys. 73 (1993) 3454–3460. https://doi.org/10.1063/1.352948.
[57] M. Dawber, J.F. Scott, Fatigue and oxygen vacancy ordering in thin-film and bulk single crystal ferroelectrics, Integr. Ferroelectr. 32 (2001) 259–266. https://doi.org/10.1080/10584580108215696.
[58] J.F. Scott, M. Dawber, Oxygen-vacancy ordering as a fatigue mechanism in perovskite ferroelectrics, Appl. Phys. Lett. 76 (2000) 3801–3803. https://doi.org/10.1063/1.126786.
[59] P. Chaudhari, Grain Growth and Stress Relief in Thin Films, J. Vac. Sci. Technol. 9 (1972) 520–522. https://doi.org/10.1116/1.1316674.

[60] S. Zhukov, Y.A. Genenko, O. Hirsch, J. Glaum, T. Granzow, H. von Seggern, Dynamics of polarization reversal in virgin and fatigued ferroelectric ceramics by inhomogeneous field mechanism, Phys. Rev. B 82 (2010), 014109. https://doi.org/10.1103/PhysRevB.82.014109.
[61] S.-C. Lu, Y.-H. Chen, W.-H. Tuan, J. Shieh, C.-Y. Chen, Effect of microstructure on dielectric and fatigue strengths of $BaTiO_3$, J. Eur. Ceram. Soc. 30 (2010) 2569–2576. https://doi.org/10.1016/j.jeurceramsoc.2010.04.028.
[62] U. Eckstein, N.H. Khansur, D. Urushihara, T. Asaka, K. Kakimoto, T. Fey, K.G. Webber, Defect modulated dielectric properties in powder aerosol deposited ceramic thick films, Ceram. Int. 48 (2022) 33082–33091. https://doi.org/10.1016/j.ceramint.2022.07.241.
[63] S.-D. Cho, J.-Y. Lee, J.-G. Hyun, K.-W. Paik, Study on epoxy/$BaTiO_3$ composite embedded capacitor films (ECFs) for organic substrate applications, Mater. Sci. Eng. B 110 (2004) 233–239. https://doi.org/10.1016/j.mseb.2004.01.022.
[64] H. Miyazaki, S. Hashimoto, N. Adach, T. Ota, Thermal expansion of ceramics around room temperature, Nagoya Institute of Technology, 2009.
[65] N.H. Khansur, U. Eckstein, K. Riess, A. Martin, J. Drnec, U. Deisinger, K.G. Webber, Synchrotron x-ray microdiffraction study of residual stresses in $BaTiO_3$ films deposited at room temperature by aerosol deposition, Scr. Mater. 157 (2018) 86–89. https://doi.org/10.1016/j.scriptamat.2018.07.045.
[66] K. Maruyama, Y. Kawakami, F. Narita, Young's modulus and ferroelectric property of $BaTiO_3$ films formed by aerosol deposition in consideration of residual stress and film thickness, Jpn. J. Appl. Phys. 61 (2022) SN1011. https://doi.org/10.35848/1347-4065/ac7d96.
[67] G. Han, J. Ryu, W.-H. Yoon, J.-J. Choi, B.-D. Hahn, J.-W. Kim, D.-S. Park, C.-W. Ahn, S. Priya, D.-Y. Jeong, Stress-controlled $Pb(Zr_{0.52}Ti_{0.48})O_3$ thick films by thermal expansion mismatch between substrate and $Pb(Zr_{0.52}Ti_{0.48})O_3$ film, J. Appl. Phys. 110 (2011) 124101. https://doi.org/10.1063/1.3669384.